Title

Three-phase Model of Visco-elastic Incompressible Fluid Flow and its Computational Implementation.

Journal

Communications in Computational Physics, 25(2)

ISSN

1815-2406

Authors

Xu, Shixin
Alber, Mark
Xu, Zhiliang

Publication Date

2019

DOI

10.4208/cicp.oa-2017-0167

Peer reviewed

Published in final edited form as:

Commun Comput Phys. 2019 ; 25(2): 586–624. doi:10.4208/cicp.oa-2017-0167.

Three-phase Model of Visco-elastic Incompressible Fluid Flow and its Computational Implementation

Shixin Xu[1], **Mark Alber**[1,2,*], **Zhiliang Xu**[2,*]

[1]Department of Mathematics, University of California, Riverside, Riverside, CA, 92521, USA

[2]Department of Applied and Computational Mathematics and Statistics, University of Notre Dame, Notre Dame, IN, 46556, USA

Abstract

Energetic Variational Approach is used to derive a novel thermodynamically consistent three-phase model of a mixture of Newtonian and visco-elastic fluids. The model which automatically satisfies the energy dissipation law and is Galilean invariant, consists of coupled Navier-Stokes and Cahn-Hilliard equations. Modified General Navier Boundary Condition with fluid elasticity taken into account is also introduced for using the model to study moving contact line problems. Energy stable numerical scheme is developed to solve system of model equations efficiently. Convergence of the numerical scheme is verified by simulating a droplet sliding on an inclined plane under gravity. The model can be applied for studying various biological or biophysical problems. Predictive abilities of the model are demonstrated by simulating deformation of venous blood clots with different visco-elastic properties and experimentally observed internal structures under different biologically relevant shear blood flow conditions.

Keywords

Phase field method; Energetic Variational Approach; multi-phase flow; visco-elasticity; variable density; slip boundary condition; deformation of blood clot; thrombus

1. Introduction

Phase field models [3, 5, 19, 28, 29, 40, 44, 46, 84, 86, 87] derived using the energy-based variational formulation, are widely used for studying multi-phase fluid flow problems. Labeling function or phase function is used in a phase field model to represent each of the phases. The sharp interface separating different species is replaced by narrow transition layer in which species mix. Free energy density functional of the labeling functions is constructed for coupling different phases. (See, among others, [3, 47, 41] for reviews of phase field approach.) A careless design of the free energy density functional may lead to meta stable states [11]. For instance, traditional pairwise combinations of double-well free energy functionals for coupling multiple fluid components may give rise to non-physical results,

*Authors for correspondence: malber@ucr.edu (Mark Alber), zxu2@nd.edu (Zhiliang Xu).

such as growth of one phase due to the presence of saddle points inside the Gibbs triangle [88].

Additional problems with deriving a phase field model arise when some fluid components are non-Newtonian. Many existing non-Newtonian flow phase field models [2, 7, 10] do not satisfy the energy dissipation law. This implies that numerical schemes designed for solving system of equations of these models likely do not to satisfy the discrete energy dissipation law either, and can result in large numerical errors [50]. These numerical errors significantly undermine accuracy of numerical model solutions over long time periods.

While most of the existing models [1, 3, 5, 17, 18, 37, 47, 52, 86, 89] focus on two-phase or Newtonian fluids, many biological and biophysical applications require multi-phase or non-Newtonian fluid flow models. There are only few existing three (or more)-phase field models [20, 45, 46, 79]. In particular, Wu and Xu [79] established the unisolvent property of coefficient matrix involved in N-phase models based on pairwise surface tensions. By using obtained matrix, authors derived an N-phase inherently invariant Cahn-Hillard model from the free energy functional. Important properties of Wu and Xu models are that the dynamics of concentrations are independent of the choice of phase variable, and the symmetric positive-definite property of the coefficient matrix can be proved equivalent to some physical condition for pairwise surface tensions. Among other multi-phase models, the model in [45] does not include components representing hydrodynamics, and models in [20, 46, 79] describe only Newtonian fluids. We use the Energy Variational Approach (EnVarA) [21, 83] to derive in this paper a novel thermodynamically consistent phase field model of three-phase incompressible fluid system with visco-elastic fluid components. Main novel modeling and numerical contributions of the paper in comparison with existing models, are as follows.

- A systematic approach is introduced to derive phase field model coupling Newtonian and Non-Newtonian fluids with large variations in densities or viscosities of individual fluid components. The Boussinesq approximation under the assumption that density ratio between two fluids is relatively small [51, 50] is not needed in our model. Components of the fluid mixture are combined in a binary tree manner [12, 73]. The feasibility of this approach is demonstrated by deriving a three-phase fluid flow model, in which two of the fluid components are visco-elastic. The resulting model can be reduced in a physically consistent manner to the two-phase model [51].
- The derived model is Galilean invariant and automatically satisfies the energy dissipation law resulting in straightforward development of an efficient and energy stable numerical scheme. All model equations are described in the Eulerian coordinate system which makes computational implementation of the model convenient. This is in contrast with many computational models coupling Navier-Stokes equations and elastic equations for simulating fluid-structure interaction problems, in which Navier-Stokes equations are solved on a fixed mesh while elastic equations are solved on the Lagrangian mesh. Computational implementation of interpolation between meshes to impose boundary condition at the fluid-structure interface is not trivial.

- Modified General Navier Boundary Condition (GNBC) [58, 59, 60] with fluid elasticity taken into account is used for solving the moving contact line problem [40, 58, 63, 77] which describes movement of an interface separating visco-elastic and pure Newtonian fluids on the solid wall.
- Efficient and energy stable numerical scheme is developed for solving the obtained model system with large variations in densities or viscosities. The model system which couples Navier-Stokes and Cahn-Hilliard equations, is solved by using combination of the energy splitting method [22, 23] and the pressure stabilization method [68].

Convergence study of the new energy stable scheme is accomplished by simulating deformation and motion of visco-elastic droplets on solid surface. Creep-relaxation test of complex fluid is used to validate the approach adopted by the model for representing visco-elasticity of the fluid. Additionally, simulations of a droplet wetting process are used to demonstrate differences between fluid visco-elasticity models which give fluid-like and solid-like behaviors, respectively.

To demonstrate the feasibility of the new model for studying biological and biophysical problems involving non-Newtonian fluids, it is applied for studying stability of venous blood clots with specific multi-component structures observed in experiments [43, 82]. Simulations of deformation of hemophilic and normal blood clots, which consist of platelet aggregates and fibrin network, under physiologically relevant shear blood flows, are shown to be in good agreement with experimental observations.

The paper is organized as follows. Section 2 describes derivation of the three-phase field model with variable densities and viscosities of fluid components. Moreover, two of the fluid components in the model are visco-elastic. An energy stable numerical scheme is introduced in Section 3 for solving model equations described in Section 2. Section 4 describes simulation results. Conclusions are provided in Section 5.

2. Derivation of the Three-phase Model using EnVarA

A three-phase model describing mixture of Newtonian and non-Newtonian fluid components is derived in this section by using binary tree approach and applying the EnVarA to ensure that the derived model satisfies the energy dissipation law. We first outline below the general idea of the EnVarA and then describe in detail steps employed to derive the three-phase model.

The EnVarA is based on the energy dissipation law [21, 26, 60, 66, 83], the Least Action Principle (LAP), the Maximum Dissipation Principle (MDP) [25, 30, 39, 53, 54, 76], and Newton’s force balance law.

Under the assumption that the system is isothermal, the model derived using the EnVarA should obey the energy dissipation law, which states that the entropy change balances with the energy dissipation

$$\frac{d}{dt}E_{total} + \Delta = 0 \Leftrightarrow \frac{d}{dt}E^{total} = -\Delta . \tag{2.1}$$

Here $E_{total} = \mathscr{K} + \mathscr{U} - T\mathscr{S} = \mathscr{K} + \mathscr{H}$ is the total energy of the system. $\mathscr{K}$ is the kinetic energy, $\mathscr{U}$ is the internal energy, T is the temperature, $\mathscr{S}$ is the entropy, and $\mathscr{H}$ is the Helmholtz free energy. Δ is the dissipation functional which is usually represented as a quadratic function of certain rates such as the fluid velocity $\boldsymbol{u}$. (Other notations used in the paper are explained in Appendix A.)

The action functional for a Hamiltonian (or conservative) system is defined as follows $A = \int_0^{t^*}\int_\Omega(\mathscr{K} - \mathscr{H})d\boldsymbol{x}dt$. The LAP states that the action functional can be optimized with respect to the flow map $\boldsymbol{x}(t) = \boldsymbol{x}(\boldsymbol{X}, t)$ (with $\boldsymbol{x}(\boldsymbol{X}, 0) = \boldsymbol{X}(t = 0)$) by taking the variation with respect to $\boldsymbol{x}$. Here $\boldsymbol{X}$ stands for the Lagrangian coordinate system, which is called the reference configuration, and $\boldsymbol{x}$ is the Eulerian coordinate, which is called deformed configuration. This gives rise to the variational derivative δA of the action functional $\delta A = \int_0^{t^*}\int_{\Omega_0}[\mathscr{F}_{con}]\cdot\delta\boldsymbol{x}d\boldsymbol{X}dt$, where $\mathscr{F}_{con}$ is the conservative force, Ω_0 is the Lagrangian reference domain of Ω, and the trajectory $\boldsymbol{x}(t)$ is the path that particle $\boldsymbol{X}$ moves from position $\boldsymbol{x}(\boldsymbol{X}, 0)$ at time $t = 0$ to position $\boldsymbol{x}(\boldsymbol{X}, t^*)$ at time $t = t^*$ [4].

The MDP states that variation of Δ with respect to certain rate (e.g., velocity $\boldsymbol{u}$) in the Eulerian coordinate system results in the dissipative force $\mathscr{F}_{dis}$, which satisfies $\delta\left(\frac{1}{2}\Delta\right) = \int_\Omega[\mathscr{F}_{dis}]\cdot\delta\boldsymbol{u}d\boldsymbol{x}$. Note that the factor $\frac{1}{2}$ is due to the underlying assumption that Δ is a quadratic function of $\boldsymbol{u}$. In the end, the equation of motion is obtained by using the force balance law, i.e., $\mathscr{F}_{con} = \mathscr{F}_{dis}$.

The rest of this section is devoted to derivation of the three-phase model describing Newtonian and non-Newtonian fluids mixture by using the EnVarA. A novel general Navier boundary condition is also introduced for imposing the wall boundary condition for studying moving contact line problem involving visco-elastic fluid. This boundary condition includes contribution of the elasticity of the non-Newtonian fluid to the contact line slip velocity.

2.1. Three-phase model derivation

We consider in this section a complex fluid mixture consisting of visco-elastic fluids A and B, and Newtonian fluid C. These three fluid components of the mixture are separated in two groups: the visco-elastic fluids mixture AB composed of fluids A and B, and the Newtonian fluid C. The volume fraction of the visco-elastic fluids mixture AB is denoted by ϕ_2 ($\phi_2 \in [0, 1]$), while the volume fraction of the fluid C is $1 - \phi_2$. Furthermore, ϕ_1 ($\phi_1 \in [0,1]$) is introduced to represent the volume fraction of fluid A in the mixture AB, and $1 - \phi_1$ is the volume fraction of fluid B in the mixture AB.

2.1.1. Definition of total energy and dissipation functionals—The total energy functional of the modeled complex fluid is defined as

$$E_{total} = \underbrace{E_{kin}}_{Macroscale} + \underbrace{E_{coh} + E_{ela} + E_w}_{Microscale}, \tag{2.2}$$

where E_{kin} is the kinetic energy, E_{coh} is the mixing energy, E_{ela} is the elastic energy, and E_w is the specific wall energy.

The kinetic energy accounts for the transport of the trinary fluid mixture and is defined as:

$$E_{kin} = \int_\Omega \left(\frac{1}{2}\rho |\boldsymbol{u}|^2\right) d\boldsymbol{x}, \tag{2.3}$$

where $\rho = \rho(\boldsymbol{x}, t) = \rho(\phi_1, \phi 2, \rho_a, \rho_b, \rho_c, t)$ is the mixture density with ρ_i being the density of phase i, $i = A, B, C,$ and $\boldsymbol{u}$ the velocity of the fluid mixture, respectively.

According to the Cahn and Hilliard approach [13], the mixing energy E_{coh} represents competition between a homogeneous bulk mixing energy density term $G(\boldsymbol{\phi})$ ('hydrophobic' part) that establishes total separation of the phases into pure components, and a gradient distortional term $\frac{|\nabla \phi|^2}{2}$ ('hydrophilic' part) that represents the nonlocal interactions between different components and penalizes spatial heterogeneity. Therefore, the mixing energy is defined as follows:

$$\begin{aligned} E_{coh} &= E_{coh1} + E_{coh2} \\ &= \int_\Omega \lambda_1 \phi_2^2 \left(G_1(\phi_1) + \frac{\gamma_1^2}{2} |\nabla \phi_1|^2 \right) d\boldsymbol{x} \\ &\quad + \int_\Omega \lambda_2 \left(G_2(\phi_2) + \frac{\gamma_2^2}{2} |\nabla \phi_2|^2 \right) d\boldsymbol{x}, \end{aligned} \tag{2.4}$$

where λ_i is the mixing energy density, γ_i is the capillary width of the interface, $G_1(\phi_1) = \alpha \phi_1^3 (\frac{\phi_1}{4} - \beta)$ [73], which has a nonzero minimum, is the hydrophobic energy of the visco-elastic mixture AB. The choice of this cohesion energy $G_1(\boldsymbol{\phi}_1)$ is for the purpose of using this model to describe complex fluids such as hydro-gel in which polymer network forms physical links and entanglements. The double well potential $G_2(\phi_2) = \frac{1}{4}\phi_2^2 (1 - \phi_2)^2$ [86] is the hydrophobic energy of the Newtonian and visco-elastic fluid mixture. In the mixing energy E_{coh1}, a factor ϕ_2^2 is included because this energy makes sense only when the volume fraction of the visco-elastic mixture AB is not zero.

To account for the visco-elastic property of the fluid mixture AB, we introduce an elastic free energy E_{ela}. In the present paper, the Kelvin-Voigt model [56] is used to describe the fluid visco-elasticity. Following the results in [49], the deformation gradient tensor $\boldsymbol{F}(\boldsymbol{X}, t)$ defined by $\boldsymbol{F}_{ij} = \frac{\partial \boldsymbol{x}_i}{\partial \boldsymbol{X}_j}$, in which $\boldsymbol{x}$ is the current (Eulerian) coordinate and $\boldsymbol{X}$ is the reference (Lagrangian) coordinate, is introduced to write the elastic energy in the Eulerian framework,

$$E_{ela} = \int_{\Omega} \frac{\lambda_{e1}\phi_2^2}{2} |\boldsymbol{F}|^2 d\boldsymbol{x} = \int_{\Omega} \frac{\lambda_{e1}\phi_2^2}{2} \mathrm{tr}\left(\boldsymbol{F}\boldsymbol{F}^T\right) d\boldsymbol{x}, \tag{2.5}$$

where $\lambda_{e1} = \lambda_{e1}(\phi_1, \lambda_A, \lambda_B)$ is the elastic energy density of non-Newtonian fluid mixture AB. λ_A and λ_B are the elastic energy density of fluids A and B, respectively. ϕ_2^2 is used to ensure that only the elasticity of the mixture AB is considered, $\mathrm{tr}(\boldsymbol{F}\boldsymbol{F}^T)$ is the trace of $\boldsymbol{F}\boldsymbol{F}^T$.

If $\nabla \cdot \boldsymbol{F}(\boldsymbol{X}, 0) = 0$ is satisfied at $t = 0$, $\nabla \cdot \boldsymbol{F} = 0$ for $t \geq 0$ by the transport equation of $\mathbf{F}$ [49]. Moreover, there exists a vector $\boldsymbol{\Psi} = (\Psi_1, \Psi_2)^T$ in the two-dimensional space [49], such that

$$\boldsymbol{F} = \begin{pmatrix} -\partial_{\boldsymbol{x}_2}\Psi_1 & -\partial_{\boldsymbol{x}_2}\Psi_2 \\ \partial_{\boldsymbol{x}_1}\Psi_1 & \partial_{\boldsymbol{x}_1}\Psi_2 \end{pmatrix}.$$

In the end, the elastic energy can be represented by using $\boldsymbol{\Psi}$ as

$$\begin{aligned} E_{ela} &= \int_{\Omega} \frac{\lambda_e}{2} |\boldsymbol{F}|^2 d\boldsymbol{x} = \int_{\Omega} \frac{\lambda_e}{2} \mathrm{tr}\left(\boldsymbol{F}\boldsymbol{F}^T\right) d\boldsymbol{x} \\ &= \int_{\Omega} \frac{\lambda_e}{2} \left(\left(\partial_{x_1}\Psi_1\right)^2 + \left(\partial_{x_2}\Psi_1\right)^2 + \left(\partial_{x_1}\Psi_2\right)^2 + \left(\partial_{x_2}\Psi_2\right)^2 \right) d\boldsymbol{x} \\ &= \int_{\Omega} \frac{\lambda_e}{2} |\nabla\Psi|^2 d\boldsymbol{x}, \end{aligned}$$

where $\lambda_e = \phi_2^2 \lambda_{e1}$.

For numerical study of the moving contact line problem [29, 40, 58, 59, 63, 64] involving the interface of fluids intersecting with the wall, a wall free energy E_w is introduced into the total energy functional to mimic the interaction between the fluid interface and the wall. The moving contact line problem studied in this paper has an interface separating the non-Newtonian fluids mixture AB from the Newtonian fluid C. The wall free energy E_w in this case is defined on the wall w and adopts the following form [84]

$$E_w = \sigma_2 \int_w f_w(\phi_2) ds, \tag{2.6}$$

where f_w is as follows:

$$f_w(\phi_2) = -\frac{(2\phi_2 - 1)\left(3 - (2\phi_2 - 1)^2\right)}{4} \cos(\theta_s). \tag{2.7}$$

Here σ_2 is the surface tension of the visco-elastic mixture and θ_s is the static contact angle [63, 64].

For the purpose of using Cahn-Hilliard equations to describe evolution of ϕ_1 and ϕ_2, the chemical potentials μ_1 and μ_2 are defined as the variational derivative of the Helmholtz free energy functional $\mathscr{H} = E_{coh} + E_{ela}$ and are as follows:

$$\mu_1 = \frac{\delta \mathscr{H}}{\delta \phi_1} = \lambda_1\left(\phi_2^2 G_1'(\phi_1) - \gamma_1^2 \nabla \cdot \left(\phi_2^2 \nabla \phi_1\right)\right) + \frac{1}{2}(\partial_1 \lambda_e)|\nabla \boldsymbol{\Psi}|^2, \tag{2.8}$$

and

$$\begin{aligned}\mu_2 = \frac{\delta \mathscr{H}}{\delta \phi_2} = \lambda_2\left(G_2'(\phi_2) - \gamma_2^2 \Delta \phi_2\right) \\ + 2\lambda_1 \phi_2\left(G_1(\phi_1) + \frac{\gamma_1^2}{2}|\nabla \phi_1|^2\right) + \frac{1}{2}(\partial_2 \lambda_e)|\nabla \boldsymbol{\Psi}|^2 .\end{aligned} \tag{2.9}$$

For the sake of simplicity, here and in the rest of the paper, ∂_i denotes ∂_{ϕ_i} for $i = 1,2$.

Remark 2.1: *There exist different definitions of the chemical potential. In papers [41, 50], the chemical potential is defined as the variational derivative of the total energy. When the mixed fluids have variable densities, there is a term* $\frac{\rho'|\boldsymbol{u}|^2}{2}$ *in the chemical potential, which is not Galilean invariant. However, as values of the mobility parameters in the Cahn-Hilliard system approach zero, the whole system converges to a Galilean invariant system. The chemical potential in [1, 34] is defined as the variational derivative of the mixing energy, which eliminates the* $\frac{\rho'|\boldsymbol{u}|^2}{2}$ *term. In our work, we define the chemical potential as the variational derivative of the sum of the mixing energy and elastic energy. This introduces the* $\frac{1}{2}(\partial_i \lambda_e)|\nabla \boldsymbol{\Psi}|^2$ *term in the chemical potentials. The reason to include the elastic energy is to ensure that the obtained system satisfies the energy dissipation law. When a complex fluid with variable elasticities is considered, it is difficult, if not impossible, to prove that the obtained system satisfies the energy dissipation law in case the elastic energy is not included in the derivation of the chemical potential. We note that, in fact, the Cahn-Hilliard type of dynamics should not be viewed strictly as a physics law. Rather, it is just a relaxation of the pure transport equation [41].*

The dissipation functional is defined as

$$\Delta = \int_\Omega \left(\frac{\eta}{2}|\mathbf{D}|^2 + M_1|\nabla \mu_1|^2 + M_2|\nabla \mu_2|^2\right) d\boldsymbol{x} + \int_w \left(\kappa|\dot{\phi}_2|^2 + \beta_s|u_s|^2\right) ds, \tag{2.10}$$

where $\eta = \eta(\phi_1, \phi_2, \eta_A, \eta_B, \eta_C, t)$ is the viscosity of the mixture, with η_i being the viscosity of phase i, $i = A, B,$ and C. M_i is the phenomenological mobility coefficient of the phase i. $\mathbf{D} = \nabla \boldsymbol{u} + (\nabla \boldsymbol{u})^T$. κ is the phenomenological relaxation time of ϕ on the wall. β_s is the slip friction coefficient, and u_s is the slip speed on the wall.

2.1.2. *Microscale transport of ϕ_1 and ϕ_2*—

We assume that ϕ_1 and ϕ_2 satisfy the following conservation laws:

$$\partial_t \phi_1 + \nabla \cdot (\boldsymbol{u} \nabla \phi_1) = 0, \tag{2.11}$$

$$\partial_t \phi_2 + \nabla \cdot (\boldsymbol{u} \nabla \phi_2) = 0. \tag{2.12}$$

Equations (2.11) and (2.12) are approximated in the phase field method by the following Cahn-Hilliard equations

$$\partial_t \phi_1 + \nabla \cdot (\boldsymbol{u} \nabla \phi_1) = \nabla \cdot (M_1 \nabla \mu_1), \tag{2.13}$$

$$\partial_t \phi_2 + \nabla \cdot (\boldsymbol{u} \nabla \phi_2) = \nabla \cdot (M_2 \nabla \mu_2). \tag{2.14}$$

In addition, $\boldsymbol{\phi}_2$ satisfies the following relaxation boundary condition on the solid wall boundary w:

$$\kappa \dot{\phi}_2 + L(\phi_2) = 0, \tag{2.15}$$

where $L(\phi_2) = \lambda_2 \gamma_2^2 \nabla_n \phi_2 + f'_w$, and $\dot{\phi}_2 = \partial_t \phi_2 + \boldsymbol{u} \cdot \nabla \phi_2$ is the material derivative of $\boldsymbol{\phi}_2$ on the wall.

2.1.3. Macroscale momentum equation—The conservative and dissipative forces are obtained by applying the LAP to the Hamiltonian part of the system and the MDP to the dissipative part of the system, respectively.

Application of the LAP yields that

$$\begin{aligned} \mathscr{F}_{con} = & -\left(\frac{1}{2}[\rho(\partial_t \boldsymbol{u} + \boldsymbol{u} \cdot \nabla \boldsymbol{u}) + (\partial_t(\rho \boldsymbol{u}) + \nabla \cdot (\rho \boldsymbol{u} \otimes \boldsymbol{u}))] + \right. \\ & + \lambda_2 \gamma_2^2 \nabla \cdot (\nabla \phi_2 \otimes \nabla \phi_2) + \lambda_1 \gamma_1^2 \nabla \cdot (\phi_2 \nabla \phi_1 \otimes \nabla \phi_1) \\ & \left. + \nabla \cdot \left(\lambda_e (\nabla \boldsymbol{\Psi})^T \nabla \boldsymbol{\Psi}\right) + \nabla P_1\right). \end{aligned} \tag{2.16}$$

By using the MDP and the flow incompressibility constraint, we obtain the following dissipative force for deriving the equation of motion in the bulk flow region

$$\mathscr{F}_{dis} = -\nabla \cdot (\eta \mathbf{D}) + \nabla P_2, \tag{2.17}$$

and the dissipative force on the wall w

$$\mathscr{F}_{dis,w} = \tau \cdot (\eta \mathbf{D}) \cdot n + \kappa \dot{\phi}_2 \partial_\tau \phi_2 + \beta_s u_s. \tag{2.18}$$

Finally, the Navier-Stokes type of equation of motion for the macroscopic trinary fluid mixture is obtained as a result of the macroscopic force balance, i.e., $\mathscr{F}_{con} = \mathscr{F}_{dis}$:

$$\begin{aligned}\frac{1}{2}[\rho(\partial_t \boldsymbol{u}+\boldsymbol{u}\cdot\nabla\boldsymbol{u})+(\partial_t(\rho\boldsymbol{u})+\nabla\cdot(\rho\boldsymbol{u}\otimes\boldsymbol{u}))] &= \nabla\cdot(\eta\mathbf{D})-\nabla\bar{P}\\ -\lambda_2\gamma_2^2\nabla\cdot(\nabla\phi_2\otimes\nabla\phi_2)-\lambda_1\gamma_1^2\nabla\cdot(\phi_2\nabla\phi_1\otimes\nabla\phi_1)&\\ -\nabla\cdot\left(\lambda_e(\nabla\boldsymbol{\Psi})^T\nabla\boldsymbol{\Psi}\right)&\end{aligned} \tag{2.19}$$

where $\bar{P}=P_1+P_2$.

The following slip boundary condition is used for the equation (2.19),

$$\beta_s u_s = -\tau\cdot\left(\eta\mathbf{D}-\lambda_e(\nabla\boldsymbol{\Psi})^T\nabla\boldsymbol{\Psi}\right)\cdot\boldsymbol{n}+L(\phi_2)\partial_\tau\phi_2\,. \tag{2.20}$$

If the elastic property of fluid is not considered, i.e., $\lambda_e = 0$, then the above slip boundary condition is reduced to the General Navier Boundary Condition (GNBC) [58, 59, 60]. In other words, the boundary condition (2.20) is a generalized form of the GNBC for the moving contact line problem involving visco-elastic fluid.

Remark 2.2: Details of using the LAP and MDP to derive the three-phase fluid model are described in Appendix B.

After the right hand side of the Navier-Stokes equation (2.19) is simplified by using the method described in Appendix B, we obtain the following three-phase Navier-Stokes Cahn-Hilliard model

$$\begin{cases}\frac{1}{2}[\rho(\partial_t\boldsymbol{u}+\boldsymbol{u}\cdot\nabla\boldsymbol{u})+(\partial_t(\rho\boldsymbol{u})+\nabla\cdot(\rho\boldsymbol{u}\otimes\boldsymbol{u}))]+\nabla P=\nabla\cdot(\eta\mathbf{D})\\ \quad -\nabla\mu_1\phi_1-\nabla\mu_2\phi_2-(\nabla\Psi)^T\nabla\cdot(\lambda_e\nabla\Psi),\\ \nabla\cdot\boldsymbol{u}=0,\\ \partial_t\Psi+\boldsymbol{u}\cdot\nabla\Psi=0,\\ \partial_t\phi_1+\nabla\cdot(\boldsymbol{u}\phi_1)=\nabla\cdot(M_1\nabla\mu_1),\\ \partial_t\phi_2+\nabla\cdot(\boldsymbol{u}\phi_2)=\nabla\cdot(M_2\nabla\mu_2),\\ \mu_1=\lambda_1\left(\phi_2^2G_1'(\phi_1)-\gamma_1^2\nabla\cdot\left(\phi_2^2\nabla\phi_1\right)\right)+\frac{1}{2}(\partial_1\lambda_e)|\nabla\Psi|^2,\\ \mu_2=\lambda_2\left(G_2'(\phi_2)-\gamma_2^2\Delta\phi_2\right)+2\lambda_1\phi_2\left(G_1(\phi_1)+\frac{\gamma_1^2}{2}|\nabla\phi_1|^2\right)\\ \quad +\frac{1}{2}(\partial_2\lambda_e)|\nabla\boldsymbol{\Psi}|^2\,.\end{cases} \tag{2.21}$$

The initial and the wall boundary conditions are given as follows:

$$\begin{cases} \boldsymbol{u}\cdot\boldsymbol{n}=0,\ \nabla_n\mu_1=\nabla_n\mu_2=0,\ \partial_n\phi_1=0 \\ \kappa\dot{\phi}_2=-L(\phi_2)=-(\varepsilon\nabla_n\phi_2+f_w'), \\ \beta_s u_s=-\tau\cdot\left[\eta\mathbf{D}-\lambda_e(\nabla\Psi)^T\nabla\Psi\right]\cdot\boldsymbol{n}+L(\phi_2)\partial_\tau\phi_2, \\ \phi_1(\cdot,0)=\phi_{10},\phi_2(\cdot,0)=\phi_{20},\Psi(\cdot,0)=\Psi_0. \end{cases} \tag{2.22}$$

Remark 2.3: This three-phase model satisfies the following conditions proposed in [11, 88]:

- *When a phase does not present in the mixture at the initial time, this phase should not appear during the time evolution of the system. E.g., if* $\phi_i(\cdot, t=0)=0$, *then* $\phi_i(\cdot, t)\equiv 0, \forall t>0$, $i=1$ *or* 2. *This is to make sure that each phase does not appear without basis.*
- *The three-phase model should be reduced to the two-phase model by setting one of the phase to be equal to zero. For example, if let* $\phi_1\equiv 1$ *and* $\lambda_e=0$, *the system* (2.21) *is reduced to the two-phase model proposed in [50].*

2.2. Energy dissipation law

The following dimensionless form of the system (2.21)–(2.22) for convenience of discussion is obtained by scaling the density, viscosity, elasticity, length and velocity by ρ_a, η_a, λ_a, L and U, respectively,

$$\begin{cases} Re\frac{1}{2}[\rho(\partial_t\boldsymbol{u}+\boldsymbol{u}\cdot\nabla\boldsymbol{u})+(\partial_t(\rho\boldsymbol{u})+\nabla\cdot(\rho\boldsymbol{u}\otimes\boldsymbol{u}))]+\nabla P \\ =\nabla\cdot(\eta\mathbf{D})-\phi_1\nabla\mu_1-\phi_2\nabla\mu_2-\alpha_e(\nabla\Psi)^T\nabla\cdot(\lambda_e\nabla\Psi), \\ \nabla\cdot\boldsymbol{u}=0, \\ \partial_t\Psi+\boldsymbol{u}\cdot\nabla\Psi=0, \\ \partial_t\phi_1+\boldsymbol{u}\cdot\nabla\phi_1=\nabla\cdot(M_1\nabla\mu_1), \\ \partial_t\phi_2+\boldsymbol{u}\cdot\nabla\phi_2=\nabla\cdot(M_2\nabla\mu_2), \end{cases} \tag{2.23}$$

where

$$\mu_1=\alpha_1\left(\frac{1}{\varepsilon_1}G_1'\phi_2^2-\varepsilon_1\nabla\cdot\left(\phi_2^2\nabla\phi_1\right)\right)+\alpha_e\frac{|\nabla\boldsymbol{\Psi}|^2}{2}\partial_1\lambda_e, \tag{2.24}$$

and

$$\begin{aligned}\mu_2 &= \alpha_2\left(\frac{1}{\varepsilon_2}G_2'-\varepsilon_2\Delta\phi_2\right)+2\alpha_1\phi_2\left(\frac{1}{\varepsilon_1}G_1+\frac{\varepsilon_1}{2}|\nabla\phi_1|^2\right) \\ &\quad+\alpha_e\frac{|\nabla\boldsymbol{\Psi}|^2}{2}\partial_2\lambda_e.\end{aligned} \tag{2.25}$$

The initial and the wall boundary conditions for the system (2.23) are given by

$$\begin{cases} \boldsymbol{u}\cdot\boldsymbol{n}=0, \quad \nabla_n\mu_1=\nabla_n\mu_2=0, \partial_n\phi_1=0 \\ \kappa\dot{\phi}_2 = -L(\phi_2), \\ l_s^{-1}u_s = -\tau\cdot\left[\eta\mathbf{D}-\alpha_e\lambda_e(\nabla\boldsymbol{\Psi})^T\nabla\boldsymbol{\Psi}\right]\cdot n+\alpha_2 L(\phi_2)\partial_\tau\phi_2, \\ \phi_1(\cdot,0)=\phi_{10}, \phi_2(\cdot,0)=\phi_{20}, \boldsymbol{\Psi}(\cdot,0)=\boldsymbol{\Psi}_0, \end{cases} \tag{2.26}$$

where the dimensionless constants are $Re=\frac{\rho_A LU}{\eta_A}$, $\varepsilon_1=\frac{\gamma_1}{L}$, $\varepsilon_2=\frac{\gamma_2}{L}$, $\alpha_1=\frac{\lambda_1\gamma_1}{\eta_A U}$, $\alpha_2=\frac{\lambda_2\gamma_2}{\eta_A U}$, $\alpha_e=\frac{\lambda_A L}{\eta_A U}$, $M_1=\frac{M_1\eta_A}{L^2}$, $M_2=\frac{M_2\eta_A}{L^2}$, and $\kappa=\frac{\kappa}{L\lambda_2\gamma_2/U}$.

One advantage of using the EnVarA is that the obtained system automatically satisfies the energy dissipation law. Theorem 2.4 states the energy dissipation law that the system (2.23)–(2.26) satisfies.

Theorem 2.4—*If ϕ_1, ϕ_2, $\boldsymbol{\Psi}$, $\boldsymbol{u}$ and P are smooth solutions of the above system* (2.23)–(2.26)*, then the following energy law is satisfied:*

$$\begin{aligned} \frac{d}{dt}\mathscr{E}_{total} &= \frac{d}{dt}(\mathscr{E}_{kin}+\mathscr{E}_{coh}+\mathscr{E}_{ela}+\mathscr{E}_w) \\ &= -\frac{\|\eta^{1/2}\mathbf{D}\|^2}{2}-M_1\|\nabla\mu_1\|^2-M_2\|\nabla\mu_2\|^2 \\ &\quad -\kappa\alpha_2\|\dot{\phi}_2\|_w^2-\|l_s^{1/2}\boldsymbol{u}_s\|_w^2, \end{aligned} \tag{2.27}$$

where $\zeta=\sqrt{\rho}$, $\mathscr{E}_{kin}=\frac{Re}{2}\|\zeta\boldsymbol{u}\|^2$,

$$\mathscr{E}_{coh}=\int_\Omega \alpha_1\phi_2^2\left(\frac{G(\phi_1)}{\varepsilon_1}+\frac{\varepsilon_1}{2}|\nabla\phi_1|^2\right)d\boldsymbol{x}+\int_\Omega\alpha_2\left(\frac{G(\phi_2)}{\varepsilon_2}+\frac{\varepsilon_2}{2}|\nabla\phi_2|^2\right)d\boldsymbol{x},$$
$$\mathscr{E}_{ela}=\alpha_e\int_\Omega\frac{1}{2}\lambda_e|\nabla\Psi|^2d\boldsymbol{x}, \text{ and } \mathscr{E}_w=\alpha_2\int_w f_w ds.$$

Proof—The main idea of the proof is to show how the left hand side of the equation (2.27) can be obtained by multiplying the Navier-Stokes equation by $\boldsymbol{u}$, the phase transport equations by μ_i, the chemical potentials by $\phi_i, i=1,2$, and the gradient of the equation for Ψ_i by $\alpha_e\lambda_e\nabla\Psi_i$, and summing them up. The dissipation terms on the right hand side of the equation (2.27) are obtained by using integration by parts and the boundary conditions specified in equations (2.26).

By using the fact that $\int_\Omega(\nabla\cdot(\rho\boldsymbol{u}\otimes\boldsymbol{u})+\rho\boldsymbol{u}\nabla\boldsymbol{u},\boldsymbol{u})d\boldsymbol{x}=0$, if we multiply the first equation of the system (2.23) by $\boldsymbol{u}$ and use integration by parts, the rate of change of kinetic energy $\frac{d}{dt}\mathscr{E}_{kin}$ is calculated

$$\begin{aligned} \frac{d}{dt}\mathscr{E}_{kin}=\frac{d}{dt}\frac{Re}{2}\|\zeta\boldsymbol{u}\|^2 &= -\frac{1}{2}\|\eta^{1/2}\mathbf{D}\|^2-(\phi_1\nabla\mu_1,\boldsymbol{u})-(\phi_2\nabla\mu_2,\boldsymbol{u}) \\ &\quad -\alpha_e\left((\nabla\boldsymbol{\Psi})^T\omega,\boldsymbol{u}\right)+(\eta\tau\cdot\mathbf{D}\cdot\boldsymbol{n},u_s)_w, \end{aligned} \tag{2.28}$$

where $\omega = \nabla \cdot (\lambda_e \nabla \boldsymbol{\Psi})$.

By taking the gradient of each component of the third equation of (2.23), the following equation is obtained

$$\partial_k(\partial_t \Psi_i) + \partial_k(\boldsymbol{u}_j \partial_j \Psi_i) = 0. \tag{2.29}$$

Inner product of above equation with $\alpha_e \lambda_e \partial_k \Psi_i$ has the form

$$\begin{aligned} & \alpha_e(\lambda_e \nabla \boldsymbol{\Psi} : \nabla(\partial_t \boldsymbol{\Psi})) \\ = \; & \alpha_e(\lambda_e \partial_k \Psi_i, \partial_k(\partial_t \Psi_i)) \\ = \; & -\alpha_e\big(\lambda_e \partial_k \Psi_i, \partial_k(u_j \partial_j \Psi_i)\big) \\ = \; & \alpha_e\big(\partial_k(\lambda_e \partial_k \Psi_i), u_j \partial_j \Psi_i\big) - \alpha_e\big(\lambda_e(\partial_k \Psi_i \partial_j \Psi_i) n_k, u_j\big)_w \\ = \; & \alpha_e\Big((\nabla \boldsymbol{\Psi})^T \omega, u\Big) - \alpha_e\Big(\tau \cdot \Big(\lambda_e (\nabla \boldsymbol{\Psi})^T \nabla \boldsymbol{\Psi}\Big) \cdot n, u_s\Big)_w. \end{aligned} \tag{2.30}$$

Adding equation (2.28) to (2.30) and using the third boundary condition in (2.26) result in the following equation

$$\begin{aligned} & \frac{d}{dt}\mathscr{E}_{kin} \\ = \; & -\frac{1}{2}\|\eta^{1/2}\mathbf{D}\|^2 - (\phi_1 \nabla \mu_1, \boldsymbol{u}) - (\phi_2 \nabla \mu_2, \boldsymbol{u}) \\ & - \alpha_e(\lambda_e \nabla \Psi, \nabla(\partial_t \Psi)) - \|l_s^{-1/2} \boldsymbol{u}_s\|_w^2 + \alpha_2(L(\phi_2)\partial_\tau \phi_2, \boldsymbol{u}_s)_w \\ = \; & -\frac{1}{2}\|\eta^{1/2}\mathbf{D}\|^2 - (\phi_1 \nabla \mu_1, \boldsymbol{u}) - (\phi_2 \nabla \mu_2, \boldsymbol{u}) \\ & - \alpha_e(\lambda_e \nabla \Psi, \nabla(\partial_t \Psi)) - \|l_s^{-1/2} \boldsymbol{u}_s\|_w^2 - \alpha_2\big(\kappa \dot{\phi}_2, \boldsymbol{u}_s \partial_\tau \phi_2\big)_w. \end{aligned} \tag{2.31}$$

Taking inner product of the fourth and fifth equations in system (2.23) with μ_1 and μ_2, respectively, results in the following system

$$(\partial_t \phi_1, \mu_1) - (\boldsymbol{u}\phi_1, \nabla \mu_1) + M_1 \|\nabla \mu_1\|^2 = 0, \tag{2.32}$$

$$(\partial_t \phi_2, \mu_2) - (\boldsymbol{u}\phi_2, \nabla \mu_2) + M_2 \|\nabla \mu_2\|^2 = 0. \tag{2.33}$$

Inner product of the chemical potential (2.24) with $-\partial_t \boldsymbol{\phi}_1$ yields

$$\begin{aligned} -(\partial_t \phi_1, \mu_1) = \; & -\alpha_1\Big(\phi_2^2 \frac{G_1'}{\varepsilon_1}, \partial_t \phi_1\Big) - \alpha_1\big(\varepsilon_1 \phi_2^2 \nabla \phi_1, \nabla(\partial_t \phi_1)\big) \\ & - \alpha_e\Big(\frac{|\nabla \boldsymbol{\Psi}|^2}{2} \partial_1 \lambda_e, \partial_t \phi_1\Big). \end{aligned} \tag{2.34}$$

Inner product of the chemical potential (2.25) with $-\partial_t \boldsymbol{\phi}_2$ and integration by parts, together with the dynamics boundary condition of $\boldsymbol{\phi}_2$ on the wall, result in the following equation

$$
\begin{aligned}
-(\partial_t\phi_2,\mu_2) &= -\frac{d}{dt}\mathscr{E}_{coh_2}-\alpha_1\left(\frac{G_1}{\varepsilon_1}+\frac{\varepsilon}{2}|\nabla\phi_1|^2,2\phi_2\partial_t\phi_2\right)\\
&\quad-\alpha_e\left(\partial_2\lambda_e\frac{|\nabla\boldsymbol{\Psi}|^2}{2},\partial_t\phi_2\right)-\alpha_2\left(\kappa\dot{\phi}_2+f'_w,\partial_t\phi_2\right)_w.
\end{aligned}
\tag{2.35}
$$

Summing up the equations (2.31)–(2.35) gives rise to

$$
\begin{aligned}
\frac{d}{dt}\mathscr{E}_{total} &= \frac{d}{dt}(\mathscr{E}_{kin}+\mathscr{E}_{coh}+\mathscr{E}_{ela}+\mathscr{E}_w)\\
&= -\frac{\|\eta^{1/2}\mathbf{D}\|^2}{2}-M_1\|\nabla\mu_1\|^2-M_2\|\nabla\mu_2\|^2\\
&\quad-\alpha_2\left(\kappa\dot{\phi}_2,\partial_t\phi_2\right)_w-\alpha_2\left(\kappa\dot{\phi}_2,u_s\partial_\tau\phi_2\right)_w-\left\|l_s^{1/2}u_s\right\|_w^2,\\
&= -\frac{\|\eta^{1/2}\mathbf{D}\|^2}{2}-M_1\|\nabla\mu_1\|^2-M_2\|\nabla\mu_2\|^2\\
&\quad-\kappa\alpha_2\|\dot{\phi}_2\|_w^2-\left\|l_s^{1/2}\boldsymbol{u}_s\right\|_w^2.
\end{aligned}
$$

■

3. Numerical Scheme for Solving Model Equations

Many techniques were proposed to improve stability and efficiency of numerical schemes for solving the Cahn-Hilliard equation [24, 35, 44, 73]. Here we use the energy convex splitting method [22, 23, 28, 29, 67, 69], which discretizes the chemical potentials related to the convex energy implicitly and the rest explicitly. Traditional projection-like methods [8, 15, 33, 72] for the variable density Navier-Stokes equations require solving an elliptic equation with variable coefficient to obtain the pressure or related scalar quantity. This is time consuming, especially when there is a large variation in fluid density. To overcome this difficulty, we choose the pressure stabilization method [29, 32, 50, 68] to solve the Navier-Stokes equation, which only involves solving pressure Poisson equation with constant coefficient and treats the divergence free condition as a penalty.

In [50], the authors proposed a decoupled scheme by introducing a half-step velocity when solving the Navier-Stokes Cahn-Hilliard system numerically. If we ignore the elastic terms in the system (2.23)–(2.26), the decoupled scheme can also be used for solving the Cahn-Hilliard equations in our model by setting the half-step velocity $\boldsymbol{u}^* = \boldsymbol{u}^n - \frac{\Delta t}{Re\rho^{n+1}}\left(\phi_1^n\nabla\mu_1^{n+1}+\phi_2^n\nabla\mu_2^{n+1}\right)$. For solving the system (2.23)–(2.26), the half-step velocity should be set to be $\boldsymbol{u}^* = \boldsymbol{u}^n - \frac{\Delta t}{Re\rho^{n+1}}\left(\phi_1^n\nabla\mu_1^{n+1}+\phi_2^n\nabla\mu_2^{n+1}-\alpha_e\left(\nabla\Psi^n\right)^T\nabla\cdot\left(\lambda_e\nabla\Psi^{n+1}\right)\right)$. However, according to the boundary conditions (2.26), it can be found that $\boldsymbol{u}^*\cdot\boldsymbol{n}$ is not zero. This means the decoupled scheme developed in [50] might not work for the system (2.23)–(2.26).

We propose in this section an efficient and energy stable scheme based on the convex splitting method [28, 29] for solving the coupled system (2.23)–(2.26) without using the half-step velocity. The first-order accurate version of the scheme is described here. Stability analysis of the scheme is described in Appendix C.

The first-order accurate energy stable scheme is constructed as follows. Given initial condition $\left(\phi_1^0, \phi_2^0, P^0, \boldsymbol{u}^0, \Psi^0\right)$, numerical solution $\left(\phi_1^{n+1}, \phi_2^{n+1}, \boldsymbol{u}^{n+1}, P^{n+1}, \boldsymbol{\Psi}^{n+1}\right)$ is updated for $n \geq 1$ by

$$\begin{cases} \dfrac{\phi_1^{n+1} - \phi_1^n}{\Delta t} + \nabla \cdot \left(\boldsymbol{u}^{n+1}\phi_1^{n+1}\right) = \nabla \cdot \left(M_1 \nabla \mu_1^{n+1}\right), \\ \dfrac{\phi_2^{n+1} - \phi_2^n}{\Delta t} + \nabla \cdot \left(\boldsymbol{u}^{n+1}\phi_2^{n+1}\right) = \nabla \cdot \left(M_2 \nabla \mu_2^{n+1}\right), \\ \partial_n \phi_1^{n+1} = 0, \\ \kappa \dot{\phi}_2^{n+1} = \kappa\left(\dfrac{\phi_2^{n+1} - \phi_2^n}{\Delta t} + \boldsymbol{u}_s^{n+1}\partial_\tau \phi_2^{n+1}\right) = -L\left(\phi_2^{n+1}\right), \end{cases} \tag{3.1a}$$

$$\begin{cases} Re\left(\dfrac{\rho^{n+1}\boldsymbol{u}^{n+1} - \rho^n \boldsymbol{u}^n}{2\Delta t} + \dfrac{1}{2}\nabla \cdot \left(\rho^{n+1}\boldsymbol{u}^{n+1} \otimes \boldsymbol{u}^n\right)\right) \\ + Re\left(\rho^n \dfrac{\boldsymbol{u}^{n+1} - \boldsymbol{u}^n}{2\Delta t} + \dfrac{\rho^{n+1}}{2}\boldsymbol{u}^n \cdot \nabla \boldsymbol{u}^{n+1}\right) \\ = -\nabla\left(2P^n - P^{n-1}\right) + \nabla \cdot \left(\eta^{n+1}\mathbf{D}\left(\boldsymbol{u}^{n+1}\right)\right) - \phi_1^{n+1}\nabla \mu_1^{n+1} \\ -\phi_2^{n+1}\nabla \mu_2^{n+1} - \alpha_e\left(\nabla \Psi^n\right)^T \nabla \cdot \left(\lambda_e^{n+1}\nabla \Psi^{n+1}\right) \\ l_s^{-1}\boldsymbol{u}_s^{n+1} = -\eta^{n+1}\tau \cdot \left[\mathbf{D}\left(\boldsymbol{u}^{n+1}\right) - \alpha_e \lambda_e^{n+1}\left(\nabla \Psi^n\right)^T \nabla \Psi^{n+1}\right] \cdot n \\ + \alpha_2 L\left(\phi_2^{n+1}\right)\partial_\tau \phi_2^{n+1}, \\ \dfrac{\boldsymbol{\Psi}^{n+1} - \boldsymbol{\Psi}^n}{\Delta t} + \boldsymbol{u}^{n+1} \cdot \nabla \boldsymbol{\Psi}^n = 0, \end{cases} \tag{3.1b}$$

$$\begin{cases} \Delta\left(P^{n+1} - P^n\right) = \dfrac{\bar{\rho}}{\Delta t} Re \nabla \cdot \boldsymbol{u}^{n+1} \\ \partial_n P^{n+1} = 0, \end{cases} \tag{3.1c}$$

where

$$\begin{aligned} \mu_1^{n+1} &= \alpha_1 \bar{\mu}_1^{n+1} - \alpha_1 \epsilon_1 \nabla \cdot \left(\left(\phi_2^{n+1}\right)^2 \nabla \phi_1^{n+1}\right) \\ &\quad + \alpha_e \frac{1}{2}\left(\left(\phi_2^{n+1}\right)^2 (1 - \alpha_{12})\right) |\nabla \boldsymbol{\Psi}^n|^2, \end{aligned}$$

$$
\begin{aligned}
\mu_2^{n+1} &= \alpha_2\bar{\mu}_2^{n+1} - \alpha_2\varepsilon_2\Delta\phi_2^{n+1} + \alpha_1\phi_2^{n+1}\varepsilon_1|\nabla\phi_1^n|^2 \\
&\quad + \alpha_e\left(\phi_2^{n+1}\left(\phi_1^n + (1-\phi_1^n)\alpha_{12}\right)\right)|\nabla\Psi^n|^2, \\
\bar{\mu}_1^{n+1} &= \frac{s_1}{\varepsilon_1}\phi_1^{n+1} - \left(\frac{s_1}{\varepsilon_1}\phi_1^n - \left(\phi_2^n\right)^2\frac{1}{\varepsilon_1}G_1'\left(\phi_1^n\right)\right), \\
\bar{\mu}_2^{n+1} &= \frac{S_2}{\varepsilon_2}\phi_2^{n+1} - \left(\frac{S_2}{\varepsilon_2}\phi_2^n - \frac{1}{\varepsilon_2}G_2'\left(\phi_2^n\right) - \frac{2\phi_2^n}{\varepsilon_1}G_1\left(\phi_1^n\right)\right), \\
\rho^{n+1} &= \rho_{13}\left(1-\phi_2^{n+1}\right) + \phi_2^{n+1}\left(\phi_1^{n+1} + \left(1-\phi_1^{n+1}\right)\rho_{12}\right), \\
\lambda_e^{n+1} &= \left(\phi_2^{n+1}\right)^2\left(\phi_1^{n+1} + \left(1-\phi_1^{n+1}\right)\alpha_{12}\right), \\
L\left(\phi_2^{n+1}\right) &= \varepsilon_2\partial_n\phi_2^{n+1} + f_w'\left(\phi_2^n\right) + \alpha_w\left(\phi_2^{n+1} - \phi_2^n\right),
\end{aligned}
$$

with $\rho_{12} = \frac{\rho_2}{\rho_1}$, $\rho_{13} = \frac{\rho_3}{\rho_1}$, $\bar{\rho} = \min(1, \rho_{12}, \rho_{13})$ and $\alpha_{12} = \frac{\lambda_B}{\lambda_A}$.

The following theorem with proof provided in Appendix C shows that the above discrete system satisfies discrete energy law.

Theorem 3.1

Let $\mathcal{N} = \max_{\phi_2^n}\left(|\frac{\sqrt{2}}{2}(2\phi_2^n - 1)\cos(\theta_s)|\right)$. *If* $\alpha_w \geq \mathcal{N}$, *and* s_1 *and* s_2 *satisfy the condition in the lemma described in Appendix C.1, then the solution* $\left(\phi_1^{n+1}, \phi_2^{n+1}, \boldsymbol{u}^{n+1}, P^{n+1}, \Psi^{n+1}\right)$ *of the scheme* (3.1) *satisfies the following discrete energy law for any* $\Delta t > 0$:

$$
\begin{aligned}
&\mathscr{E}^{n+1} + \frac{(\triangle t)^2}{2\bar{\rho}Re}\|\nabla P^{n+1}\|^2 + \Delta t\left(\frac{1}{2}\left\|\eta^{1/2}\mathbf{D}\left(\boldsymbol{u}^{n+1}\right)\right\|^2\right) \\
&+ \Delta t\left(\left\|M_1^{1/2}\nabla\mu_1\right\|^2 + \left\|M_2^{1/2}\nabla\mu_2\right\|^2\right) \\
&+ \Delta t\left(\left\|l_s^{-1/2}\boldsymbol{u}_s^{n+1}\right\|_w^2 + \kappa\alpha_2\left\|\dot{\phi}_2^{n+1}\right\|_w^2\right) \\
\leq\ &\mathscr{E}^n + \frac{(\Delta t)^2}{2\bar{\rho}Re}\|\nabla P^n\|^2
\end{aligned}
\tag{3.2}
$$

Remark 3.2

In the actual numerical implementation, we use finite element method to discretize the space. The nonlinear terms $\nabla\cdot(\boldsymbol{u}\boldsymbol{\phi}_i)$ *are discretized in time as* $\nabla\cdot\left(\boldsymbol{u}^n\phi_i^{n+1}\right)$ *to make the resulting numerical equations easy to solve [29]. Even though this treatment introduces a CFL-like constraint for choosing the time step size* Δt, *it decouples the system* (3.1) *into three independent subsystems. This makes the numerical implementation much easier than implementation which involves solving a large nonlinear system by iteration method. Moreover,* $\left(\phi_2^{n+1}, \mu_2^{n+1}\right)$ *is updated by using the nth step information on the numerical implementation before computing other unknowns. Then they are used to update* $\left(\phi_1^{n+1}, \mu_1^{n+1}\right)$. ($\boldsymbol{\Psi}^{n+1}$, $\boldsymbol{u}^{n+1}$, p^{n+1}) *are calculated in the end.*

4. Simulation Results

4.1. Droplet sliding on an inclined plane under gravity

Dynamics of a droplet sliding on an inclined plane under gravity [64, 65, 80] is used in this subsection to demonstrate convergence of the numerical scheme proposed in the previous section. The gravitational force ρG is added to the right hand side of the Navier-Stokes equation. Initial profile of the droplet is chosen in the form of a circular cap with contact angle 90°. Computational domain is chosen to be [0, 1.5] × [0, 0.5]. (See also Fig. 1.)

Droplet in this study is treated as a two-phase fluid. The droplet and the ambient fluid surrounding the droplet make the three-phase system. Densities of the two fluid components of the droplet are $\rho_A = \rho_B = 10^3 kg/m^3$, their viscosities are $\eta_A = \eta_B = 100 cP$, and elasticities are $\lambda_A = 1 Pa$, $\lambda_A = 0.5 Pa$ respectively. The density ratio of the droplet to the ambient fluid is 1000 and the viscosity ratio is 10. Values of non-dimensional parameters corresponding to the characteristic length $L = 1 \times 10^{-3} m$ and velocity $U = 1 \times 10^{-2} m/s$, are listed in Table 1. The static contact angle of the droplet is 90°, and the inclination angle of the wall is $\alpha = 45°$. Evolution of the advancing contact point x_a and the receding contact point x_r of the droplet from the initial time $t = 0$ to the time $t = 5$ was computed using three different meshes with mesh sizes $h = 1/64$, 1/128 and 1/256, respectively. Fig. 2 demonstrates convergence of the numerical solution computed by the proposed numerical scheme.

4.2. Creep-recovery test

The Kelvin-Voigt model [42, 56] is used to represent behavior of a solid-like material undergoing reversible, visco-elastic deformation. Namely, the material described by the Kelvin-Voigt model deforms at a decreasing rate, and approaches asymptotically the steady-state strain under a constant stress. When the stress is released, the material gradually relaxes towards it initial un-deformed configuration. However, complete recovery to the initial configuration is never achieved in finite time. This is called creep-recovery.

In this section, we use a half circular-shaped droplet on a plane to do the creep-recovery test numerically. The droplet is surrounded by a constant shear Newtonian flow. Values of non-dimensional parameters corresponding to the characteristic length $L = 1 \times 10^{-3} m$ and velocity $U = 1 \times 10^{-2} m/s$ are the same as ones listed in Table 1. Computational domain is chosen to be [0, 1.5] × [0, 0.5]. From the time $t = 0$ to $t = 1$, a constant inlet flow condition with velocity $v = 20(0.5 - y)y$ is added on the left of the boundary. After $t = 1$, the inlet flow is stopped and the droplet gradually recovers.

In Fig. 3, we show the creep-recovery test result. It shows that before $t = 1$, the droplet strain increases monotonically, i.e., the droplet undergoes creep process. After $t = 1$, the droplet strain decreases with time to a constant value, which is called permanent deformation due to dissipation of the system. Snapshots of the droplet profiles are presented in Fig. 4. The largest permanent deformation is around the left comer of the droplet. This is caused by the dissipation on the boundary with rate $\kappa\alpha_2|\dot{\phi}_2|^2$ See also Theorem 2.4. This numerical study confirms that our model produces visco-elastic behavior of the fluid described by the Kelvin-Voigt model.

In the next section, we compare simulations by using the Oldroyd-B and Kelvin-Voigt models for describing fluid visco-elasticity to reveal their differences.

4.3. Droplet spreading test for Oldroyd-B and Kelvin-Voigt models

As we mentioned in the previous section, the Kelvin-Voigt model is used for describing behavior of solid-like visco-elastic materials. For fluid-like visco-elastic materials, one of the most popular model is the Oldroyd-B model [9, 27, 77, 85, 90]. Conceptually, the Oldroy-B model is constructed by connecting a spring and a dashpot sequentially. The deformation of the spring is finite, while the dashpot retains deformation when the load is removed. Therefore, a material described by the Oldroyd-B model is more like a fluid than a solid.

In this section, we describe simulations of a droplet spreading on a plane, with its visco-elastic property described by the Kelvin-Voigt model and the Oldroy-B model, respectively. We also simulate a pure Newtonian droplet spreading for comparison. Initial shapes of these droplets are all chosen to be a half circle with radius 0.2 and center (0.75, 0). Other parameters values are the same as those in [77]. Computational domain is chosen to be [0, 1.5] × [0, 0.5]. For the Oldroyd-B model simulation, we use the equation (***6***) in [77] to describe evolution of the visco-elastic tensor, and couple it with the Cahn-Hilliard Navier-Stokes equations in our model.

Fig. 5 shows the interface profiles of these droplets at different times. It can be seen that the Oldroyd-B droplet (blue dash line) spreads much faster than the pure Newtonian droplet (black line) before $t = 1.5$. After that, the spreading speed of the pure Newtonian droplet is greater than the Oldroyd-B droplet as observed in [77]. The Kevin-Voigt droplet (red dash dot line) spreads slower than the pure Newtonian droplet as expected.

The dynamics of contact angles of different type droplets are shown in Fig. 6(a). The results shows the contact angles quickly decay from initial 150° to 60° and then slowly approach equilibrium angle 45°. Fig. 6(b) describes evolution of spreading radius, which is defined as the distance between two contact points. The Oldroyd-B droplet and the pure Newtonian droplet achieve the same spreading radius (d = 0.8146) when they reach steady state. While the spreading radius of the Kelvin-Voigt droplet (d = 0.776) is 5% smaller than the pure Newtonian droplet. This result is consistent with the findings in [77]. Thus our simulations also showed importance of including physical properties of fluids when studying its dynamics. Moreover, when the Weissenberg number $Wi = \lambda_O U/L$, which compares elastic force to viscous force, where λ_0 is the relaxation time in the Oldroyd-B model, increases from 2 to 5, the Oldroyd-B droplet spreading speed also increases. For the Kevin-Voigt droplets, the spreading speeds decrease with increasing shear modulus.

4.4. Deformation of Venous Blood Clot under Shear Flow

To demonstrate applicability and relevance of the novel three-phase model introduced in this paper for studying variety of problems in science and engineering, the model has been applied for studying the role of mechanical properties of a blood clot formed in a vein [82] in determining its stability under biologically relevant flow conditions. This is an important

biomedical problem for many reasons. For example, fragile blood clot may break to form several large pieces, or emboli, which can end up in lungs and subsequently cause fatal outcomes for patients [14]. Also, hemophilia patients suffer from bleeding disorder, which is partially attributed to the mechanical properties of the clots. Fibrin networks in a hemophilic clot are more sparse than in a clot formed in normal blood, and they are less resistent to the shear stress generated by the blood flow [43]. The three-phase model simulations presented here reveal how changes in bulk properties of blood clots result in different responses of normal and hemophilic blood clots to the blood flow. Parameter values of elasticities of blood clot components in our simulations used the experimental data provided in Tables 4 and 5 of Section 3 of reference [43].

For simplicity, we consider stability of small blood clots formed in micron size blood venules. We assume that a blood clot, which is a porous and visco-elastic gel type substance, consists of three major components: plasma, fibrin network and platelet aggregates. (See Fig. 7(a) for an example of its structure.) Fibrin network is composed of thin fibers [31, 75]. Platelet aggregates are formed by the activated platelets, which change their shapes after activation and tightly adhere with each other [36, 91]. Experimental image Fig. 7(b) shows that stabilized non-occluding blood clot formed in vein has a dense core (in yellow color) consisting mainly of aggregates of activated platelets and fibrin network. A porous shell (in green color) which covers the core, has high concentration of fibrin network and low concentration of platelets. This clot structure was used as the initial structure for clot simulations presented in this section.

Fibrin network and platelet aggregates are treated in the model as visco-elastic fluids, and plasma is treated as a Newtonian fluid. The initial value of the volume fraction of the simulated blood clot (ϕ_2) is set to be close to 1 and 0.7 in the core and shell regions, respectively. Initial values of the volume fraction of platelets (ϕ_1) are 0.7 and 0.5 in the core and shell regions of the simulated blood clot, respectively. The maximum volume fraction of the fibrin network is assumed to occur near the surface of the clot (Fig. 7(f)) to mimic the fiber cap observed in the experiments [43, 48]. Fig. 7(d–f) shows the initial distributions of the volume fractions of components of the simulated clot, which correspond to the experimental observations described in [48]. Small spike-like extensions on the surface of the clot, which are similar to the ones seen in experimental figures (8–9) from [81], are added to the initial surface of the simulated blood clot to represent its surface in more realistic way.

Computational domain is chosen to be $[0, L_x] \times [0, L_y]$, where $L_x = 800 \times 10^{-6} m$ and $L_y = 320 \times 10^{-6} m$ are the length and width of the domain, respectively. The inlet flow velocity imposed on the left boundary of the domain is given by $\mathbf{u}_{in} = \left(4u_{max}\frac{y(L_y - y)}{L_y^2}, 0\right)$, where $u_{max} = 3.2 \times \boldsymbol{10^{-2}}$m/s. (See also Fig. 7(c).) Based on the experimental results in [57, 74], we assume that densities of the plasma and the blood clot are both $\rho = 1.025 \times 10^3 kg/m^3$. Adhesion between blood clot and vessel wall [70, 71, 78] prevents the blood clot from moving on the vessel wall. Therefore, the no-slip boundary condition is used for the Navier-Stokes equations in the simulations.

The viscosity of the fibrin network η_n in a hemophilia clot is varied in simulations between $4cP$ and $40cP$ [55]. The viscosity of the platelet aggregate η_p is chosen to be $40cP$ [38]. Also, the viscosity of the fibrin network in a normal clot is set to be $400cP$, and the viscosity of the platelet aggregate is varied between $40cP$ and $400cP$ [38, 62]. The viscosity of the plasma is assumed to be $\eta_f = 4cP$ [81]. The elastic modulus λ_n of the fibrin network of hemophilia clots is about $\mathcal{O}(1Pa)$ [43]. The elastic modulus of the fibrin network generated by using normal blood varies between $\mathcal{O}(10Pa)$ and $\mathcal{O}(100Pa)$ [43]. Simulations are stopped when no blood clot deformation is detected.

Panels (a-b) of the Fig. 8 demonstrate that small spike-like extensions, which mainly consist of fibrin, on the surface of a hemophilia clot develop into extensively elongated thin structures (emboli) (breakup of the emboli is not shown); while panels (c-d) of the Fig. 8 show that normal clots deform only slightly. The simulations reveal a possible novel mechanism of destabilization of a hemophilia clot. Since surfaces of clots in general are not smooth, emboli can develop by the fibrin network on hemophilia clot surface even under normal blood flow conditions, and subsequently detach from the clot. This makes formation of a stable clot in hemophilia blood much harder than in normal blood. Simulations also predict that size of hemophilia clot was significantly smaller than normal clot. Volume changes of normal (red circles) and hemophilia (blue triangles) clots with respect to time are shown in Fig. 8e. The volume of the hemophilia clot gradually decreases after $0.5s$ by flow removal of the emboli and reaches a constant value around $1s$, which is about 28.9% of its initial volume. On the other hand, the volume of the normal clot almost does not change. This is consistent with the experimentally observed clots [55]. Note that our simulation did not consider blood clot growth. This is why size of the simulated hemophilia clot reaches a constant value around $1s$.

Simulations were used to study effects of changes in elasticity of the fibrin network on clot stability. The following values of the elasticity modulus of the fibrin network [43] are used in simulations: $0.1Pa$, $1Pa$, $10Pa$ and $50Pa$. Viscosities of the fibrin network and platelet aggregate are fixed at $40cP$. Fig. 9 shows that the clot with $0.1Pa$ elasticity modulus of the fibrin network is stretched to form a long and thin tail. When value of the elasticity modulus of the fibrin network increases, the clot becomes less deformable. This is consistent with the results in [43], and shows how elasticity of fibrin network affects clot deformation. Note that viscosities of the fibrin network and platelet aggregate used in these simulations are for hemophilia clots. Our simulations predicted that compared with viscosities of the fibrin network and platelet aggregate, the elasticity of the fibrin network played major role in resisting clot deformation induced by blood flow.

Fig. 10 shows that increase of fibrin network elasticity decreases the average speed of the intrathrombous flow, which also indicates that clot is less deformable. Simulations described in this section suggest that clots forming in hemophilia patients can develop emboli resulting in them being much less stable then clots developing in healthy individuals.

5. Conclusions

Novel thermodynamically consistent three-phase Navier-Stokes Cahn-Hilliard model for simulating complex fluids is presented in the paper. The new model which is derived by using the EnVarA, is shown to be capable of simulating fluids with large density and viscosity ratios, and satisfy the energy dissipation law. Energy stable numerical scheme is also developed to solve obtained system of model equations. Convergence of the numerical scheme is demonstrated by simulating droplet sliding on an inclined plane. Modified General Navier Boundary Condition with fluid elasticity taken into account is introduced for purpose of simulating contact line problems.

Differences between outcomes obtained using Kelvin-Voigt and Oldroyd- B models representing visco-elasticity of complex fluids axe studied by using creep-recovery test for fluids and droplet spreading. Simulations suggest that the Kelvin-Voigt model is suitable for modeling complex fluid with reversible, visco-elastic deformation. While the Oldroyd-B model is more suitable for modeling complex fluid with fluid-like behavior.

Obtained model was used for studying deformation and stability of micron size blood clots under physiologically relevant blood flow conditions. Blood clot simulations showed that hemophilia clots are more deformable and unstable than blood clots obtained using normal blood [55]. Model simulations revealed that different responses of hemophilia and normal clots to blood flow are partially due to different structures and densities of fibrin networks. Notice that the viscosity and elasticity of platelet aggregates were varied in simulations as well.

The three-phase model can be generalized to study lysis (disintegration) of a blood clot due to activity of thrombolytic agents. It has been shown in [70, 71] that intra-thrombus molecular transport is affected by the structure of the blood clot. Therefore the model described in this paper can be coupled with the anti-coagulation transport sub-models to predict conditions of the gradual resolution of a blood clot [6].

Our model includes three phases. It can be viewed as a special case of the models described in the reference [79] with additional modification. This modification was motivated by the fact that for N-phase ($N > 3$) system, the surface tension between two phases cannot be uniquely represented by phase specific surface tension. Many previous works let surface tensions be homogeneous in this situation. In order to include non-homogeneous surface tensions and ensure no phase appears artificially, we couple phases hierarchically. Namely, the phase function in our model is treated not in a pairwise way but by using the binary tree approach. The binary tree approach is used to avoid deriving complicated algebraic relations between pairwise surface tension and phase specific surface tension for $N \geq 3$ phases. Note that our model also satisfies Assumptions 2 and 3 in [79]. Moreover, the mixing energy as $\Lambda = \begin{bmatrix} \phi_2^2 & 0 \\ 0 & 1 \end{bmatrix}$ described in our paper is a generation of the case $\Lambda = I$ described in [79]. Therefore, our binary tree approach provides a simple alternative for coupling N-phase ($N \geq 3$) fluids.

Acknowledgments

The authors would like to thank Professor Chun Liu from Penn State University for discussion of the application of the Energetic Variational Approach for the derivation of the model. This research was partially supported by the NSF grant DMS-1517293 and NIH grant IU01HL116330.

Appendix A. Mathematical notations used in the paper

Mathematical notations used in this paper are as follows. Suppose a 2-rank tensor is denoted as $\boldsymbol{F}$, its l_2 norm is $|\boldsymbol{F}|^2 = \sum_{ij=1,2} F_{ij}^2$. If A and B are two 2-rank tensors, then $(AB)_{ij} = \sum_k A_{ik}B_{kj}$ and the double dot product of these two tensors is $\mathbf{A}:\mathbf{B} = \sum_{ij} A_{ij}B_{ij}$. If a and b are two vectors, the outer product $a \otimes b$ means $(a \otimes b)_{ij} = a_i b_j$. L^2 norm of the smooth function f in the domain Ω, $\left(\int_\Omega |f|^2 d\boldsymbol{x}\right)^{1/2}$, is denoted by $/\!/f/\!/_\Omega$ and the L^2 norm on the boundary w, $\left(\int_\Gamma |f|^2 ds\right)^{1/2}$, is denoted by $/\!/f/\!/_w$. If f and g are two smooth functions in Ω, (f, g) stands for the inner product of these two functions and it is defined by $(f, g) = \int_\Omega fg d\boldsymbol{x}$.

Appendix B. Derivation of the three-phase model

We first use LAP to derive the conservative force. The action functional is defined as follows:

$$\begin{aligned}\mathscr{A} &= \int_0^{t^*}\int_\Omega \frac{1}{2}\rho|\boldsymbol{u}|^2 - \int_0^{t^*}\int_\Omega \lambda_1\phi_2^2\left(G_1(\phi_1) + \frac{\gamma_1^2}{2}|\nabla\phi_1|^2\right)d\boldsymbol{x} \\ &\quad - \int_0^{t^*}\int_\Omega \lambda_2\left(G_2(\phi_2) + \frac{\gamma_2^2}{2}|\nabla\phi_2|^2\right)d\boldsymbol{x} - \int_0^{t^*}\int_\Omega \frac{\lambda_e}{2}|\nabla\boldsymbol{\Psi}|^2 d\boldsymbol{x}\,.\end{aligned} \tag{B.1}$$

We use 1-parameter family of volume preserving diffeomorphisms to perform the variation $\boldsymbol{x}^\varepsilon$, such that $\boldsymbol{x}^0 = \boldsymbol{x}$ and $\frac{d\boldsymbol{x}^\varepsilon}{d\varepsilon}|_{\varepsilon=0} = \boldsymbol{y}$, where $\boldsymbol{y}$ is smooth function with compact support and satisfies $\boldsymbol{y}(X, 0) = \boldsymbol{y}(X, t^*) = 0$ for any $X \in \Omega_0$. For any ε, $\boldsymbol{x}^\varepsilon$ is required to satisfy $\det \frac{\partial \boldsymbol{x}^\epsilon}{\partial \boldsymbol{X}} = 1$. This leads to the divergence free condition for $y(\boldsymbol{X}, t) = \tilde{y}(\boldsymbol{x}(\mathbf{X}, t), t)$, i.e. $\nabla_{\boldsymbol{x}} \cdot \tilde{\boldsymbol{y}} = 0$. For LAP, we use the variations $\boldsymbol{x}^\varepsilon$ of $\boldsymbol{x}$ as described above. The variation of action functional $\mathscr{A}$ is calculated as follows:

$$
\begin{aligned}
&\frac{d}{d\varepsilon}|_{\varepsilon=0} A(\boldsymbol{x}^{\epsilon}) \\
=\ & \frac{d}{d\varepsilon}|_{\varepsilon=0} \int_0^{t^*} \int_{\Omega_0} \left(\frac{\rho(\phi_{10}(\boldsymbol{X}), \phi_{20}(\boldsymbol{X}))}{2} |\boldsymbol{x}_t|^2 \right) d\boldsymbol{X} dt \\
&- \frac{d}{d\varepsilon}|_{\varepsilon=0} \int_0^{t^*} \int_{\Omega_0} \left(\lambda_1 \phi_{20}(\boldsymbol{X}) \left(G_1(\phi_{10}) + \frac{\gamma_1^2}{2} |\boldsymbol{F}^{-T} \nabla_{\boldsymbol{X}} \phi_{10}(\boldsymbol{X})|^2 \right) \right) d\boldsymbol{X} dt \\
&- \frac{d}{d\varepsilon}|_{\varepsilon=0} \int_0^{t^*} \int_{\Omega_0} \left(\lambda_2 \left(G_2(\phi_{20}(\boldsymbol{X})) + \frac{\gamma_2^2}{2} |\boldsymbol{F}^{-T} \nabla_{\mathbf{X}} \phi_{20}(\boldsymbol{X})|^2 \right) \right) d\boldsymbol{X} dt \\
&- \frac{d}{d\varepsilon}|_{\varepsilon=0} \int_0^{t^*} \int_{\Omega_0} \left(\frac{1}{2} \lambda_e(\phi_0(\boldsymbol{X})) |\nabla_{\mathbf{X}} \Psi_0 \boldsymbol{F}^{-1}|^2 \right) d\boldsymbol{X} dt \\
=\ & I_1 + I_2 + I_3 + I_4 .
\end{aligned}
\tag{B.2}
$$

Here $\phi_i(x) = \frac{\phi_{i,0}}{\det \boldsymbol{F}}$ [83], for $i = 1, 2$, is used, $\det \boldsymbol{F} = 1$ for the incompressible fluid.

This yields the following form of the first term of the right hand side of equation (B.2)

$$
\begin{aligned}
I_1 &= \int_0^{t^*} \int_{\Omega_0} \rho(\phi_{10}, \phi_{20}) \boldsymbol{x}_t \boldsymbol{y}_t d\boldsymbol{X} dt \\
&= -\int_0^{t^*} \int_{\Omega_0} \rho(\phi_{10}, \phi_{20}) (\boldsymbol{x}_{tt} \boldsymbol{y}) d\boldsymbol{X} dt \\
&= -\int_0^{t^*} \int_{\Omega} \rho(\phi_1, \phi_2) (\partial_t \boldsymbol{u} + \boldsymbol{u} \cdot \nabla \boldsymbol{u}, \tilde{\boldsymbol{y}}) d\boldsymbol{x} dt .
\end{aligned}
\tag{B.3}
$$

At the same time,if we draw back from Lagrangian to Eulerian and then do the integration by parts, we have

$$
\begin{aligned}
I_1 &= \int_0^{t^*} \int_{\Omega_0} \rho(\phi_{10}, \phi_{20}) \boldsymbol{x}_t \boldsymbol{y}_t d\boldsymbol{X} dt \\
&= \int_0^{t^*} \int_{\Omega} \rho(\phi_1, \phi_2) (\boldsymbol{u}, \tilde{\boldsymbol{y}}_t + \boldsymbol{u} \cdot \tilde{\boldsymbol{y}}_t) d\boldsymbol{x} dt \\
&= -\int_0^{t^*} \int_{\Omega} (\partial_t (\rho \boldsymbol{u}) + \nabla \cdot (\rho \boldsymbol{u} \otimes \boldsymbol{u}), \tilde{\boldsymbol{y}}) d\boldsymbol{x} dt .
\end{aligned}
\tag{B.4}
$$

In this work, we combine above two formula as shown in [41]

$$
\begin{aligned}
I_1 = & -\int_0^{t^*} \int_{\Omega} \left(\frac{1}{2} \rho(\partial_t \boldsymbol{u} + \boldsymbol{u} \cdot \nabla \boldsymbol{u}), \tilde{\boldsymbol{y}} \right) d\boldsymbol{x} dt \\
& - \int_0^{t^*} \int_{\Omega} \left(\frac{1}{2} (\partial_t (\rho \boldsymbol{u}) + \nabla \cdot (\rho \boldsymbol{u} \otimes \boldsymbol{u})), \tilde{\boldsymbol{y}} \right) d\mathbf{x}
\end{aligned}
\tag{B.5}
$$

$\frac{d\boldsymbol{F}^{\epsilon}}{d\varepsilon}|_{\varepsilon=0} = -\boldsymbol{F}^{-1} (\nabla_{\mathbf{X}} \boldsymbol{y}) \boldsymbol{F}^{-1}$[26] results in the following form of the second and third terms

$$
\begin{aligned}
I_2 &= -\int_0^{t^*}\int_{\Omega_0}\lambda_1\gamma_1^2\phi_{20}\Big(\boldsymbol{F}^{-T}\nabla_{\mathbf{X}}\phi_{10}(\boldsymbol{X}),\Big(-\boldsymbol{F}^{-T}(\nabla_{\boldsymbol{X}}y)^T\boldsymbol{F}^{-T}\nabla_{\boldsymbol{X}}\phi_{10}\Big)\Big)d\boldsymbol{X}dt \\
&= -\int_0^{t^*}\int_{\Omega}\lambda_1\gamma_1^2(\phi_2\nabla\phi_1,(-\nabla\tilde{y}\nabla\phi_1))d\boldsymbol{x}dt \\
&= -\int_0^{t^*}\int_{\Omega}\Big(\lambda_1\gamma_1^2\nabla\cdot(\phi_2\nabla\phi_1\otimes\nabla\phi_1)\Big)\tilde{y}d\boldsymbol{x}dt\,.
\end{aligned}
\tag{B.6}
$$

$$
I_3 = -\int_0^{t^*}\int_{\Omega}\Big(\lambda_2\gamma_2^2\nabla\cdot(\nabla\phi_2\otimes\nabla\phi_2)\Big)\tilde{y}d\boldsymbol{x}dt\,. \tag{B.7}
$$

The fourth term are transformed in a similar way as follows

$$
\begin{aligned}
I_4 &= -\int_0^{t^*}\int_{\Omega_0}\lambda_e(\phi_{10},\phi_{20})\Big((\nabla_{\boldsymbol{X}}\Psi_0)\boldsymbol{F}^{-1}:\Big(-(\nabla_{\boldsymbol{X}}\Psi_0)\boldsymbol{F}^{-1}(\nabla_{\boldsymbol{X}}y)\boldsymbol{F}^{-1}\Big)\Big)d\boldsymbol{X}dt \\
&= -\int_0^{t^*}\int_{\Omega}\lambda_e(\phi_1,\phi_2)(\nabla\Psi:(-\nabla\Psi\nabla\tilde{y}))d\boldsymbol{x}dt \\
&= -\int_0^{t^*}\int_{\Omega}\Big(\nabla\cdot\Big(\lambda_e(\phi)(\nabla\Psi)^T\nabla\Psi\Big),\tilde{y}\Big)d\boldsymbol{x}dt\,.
\end{aligned}
\tag{B.8}
$$

Combining formula from (B.5) to (B.8), and taking into account of the incompressibility and the Weyl's decomposition or Helmholtz's decomposition, for some $P_1 \in W^{1,2}(\Omega)$ yields

$$
\begin{aligned}
\mathscr{F}_{con} = &-\Big(\Big[\frac{1}{2}\rho(\partial_t\boldsymbol{u}+\boldsymbol{u}\cdot\nabla\boldsymbol{u})+\frac{1}{2}(\partial_t(\rho\boldsymbol{u})+\nabla\cdot(\rho\boldsymbol{u}\otimes\boldsymbol{u}))\Big]+ \\
&+\lambda_2\gamma_2^2\nabla\cdot(\nabla\phi_2\otimes\nabla\phi_2)+\lambda_1\gamma_1^2\nabla\cdot(\phi_2\nabla\phi_1\otimes\nabla\phi_1) \\
&+\nabla\cdot\Big(\lambda_e(\nabla\Psi)^T\nabla\Psi\Big)+\nabla P_1\Big).
\end{aligned}
$$

Variation of the dissipation functional with respect to $\boldsymbol{u}^{\varepsilon}=\boldsymbol{u}+\varepsilon\mathrm{v}$ with $\nabla\cdot v=0$ in Ω and $v\cdot\boldsymbol{n}=0$ on the wall w, where $\boldsymbol{n}$ is an outer normal vector of the wall, in the Eulerian coordinate system is as follows

$$
\frac{1}{2}\frac{\delta\Delta}{\delta\boldsymbol{u}}=\int_{\Omega}(-\nabla\cdot(\eta\mathbf{D}))vd\boldsymbol{x}+\int_{w}\Big(\tau\cdot(\eta\mathbf{D})\cdot n+\kappa\dot{\phi}_2\nabla_{\tau}\phi_2+\beta_s\boldsymbol{u}_s\Big)v_{\tau}ds, \tag{B.9}
$$

where $v_{\tau}=\mathbf{v}\cdot\boldsymbol{\tau}$ and $\boldsymbol{\tau}$ is a tangential vector to the wall. The following expressions are also taken into account $\boldsymbol{u}\cdot\boldsymbol{\tau}=u_s$ and $\dot{\phi}=\partial_t\phi_2+\boldsymbol{u}_s\partial_{\tau}\phi_2$. The following expression for the dissipative force in the equation of motion in the bulk region is obtained using MDP and the incompressible constraint

$$
\mathscr{F}_{dis}=-\nabla\cdot(\eta\mathbf{D})+\nabla P_2\,. \tag{B.10}
$$

Finally, after using the force balance in the bulk region, *i.e.*, $\mathscr{F}_{con}=\mathscr{F}_{dis}$, we obtain the equation of motion for the macroscopic fluid mixture

$$\begin{aligned}&\frac{1}{2}[\rho(\partial_t \boldsymbol{u}+\boldsymbol{u}\cdot\nabla\boldsymbol{u})+(\partial_t(\rho\boldsymbol{u})+\nabla\cdot(\rho\boldsymbol{u}\otimes\boldsymbol{u}))]\\ =\;&\nabla\cdot(\eta\mathbf{D})-\nabla\bar{P}-\lambda_2\gamma_2^2\nabla\cdot(\nabla\phi_2\otimes\nabla\phi_2)\\ &-\lambda_1\gamma_1^2\nabla\cdot(\phi_2\nabla\phi_1\otimes\nabla\phi_1)-\nabla\cdot\left(\lambda_e(\nabla\boldsymbol{\Psi})^T\nabla\boldsymbol{\Psi}\right),\end{aligned}\tag{B.11}$$

where $\bar{P}=P_1-P_2$. The right hand side terms of the previous equation can be written

$$\begin{aligned}&\lambda_1\gamma_1^2\nabla\cdot(\phi_2(\nabla\phi_1\otimes\nabla\phi_1))\\ =\;&\lambda_1\gamma_1^2\nabla\cdot(\phi_2\nabla\phi_1)\nabla\phi_1+\frac{\gamma_1^2}{2}\lambda_1\phi_2\nabla|\nabla\phi_1|^2\\ =\;&-\lambda_1\left(-\gamma_1^2\nabla\cdot(\phi_2\nabla\phi_1)+\phi_2G_1'(\phi_1)\right)\nabla\phi_1+\lambda_1\phi_2\nabla\left(G_1(\phi_1)+\frac{\gamma_1^2}{2}|\nabla\phi_1|^2\right)\\ =\;&-\mu_1\nabla\phi_1+\lambda_1\phi_2\nabla\left(G_1(\phi_1)+\frac{\gamma_1^2}{2}|\nabla\phi_1|^2\right)+\left(\partial_1\lambda_e\frac{1}{2}|\nabla\boldsymbol{\Psi}|^2\right)\nabla\phi_1,\end{aligned}$$

$$\begin{aligned}&\lambda_2\gamma_2^2\nabla\cdot(\nabla\phi_2\otimes\nabla\phi_2)\\ =\;&\lambda_2\gamma_2^2\Delta\phi_2\nabla\phi_2+\frac{\gamma_2^2\lambda_2}{2}\nabla|\nabla\phi_2|^2\\ =\;&-\lambda_2\left(-\gamma_2^2\Delta\phi_2+G_2'(\phi_2)\right)\nabla\phi_2+\lambda_2\nabla\left(\frac{\gamma_2^2}{2}|\nabla\phi_2|^2+G_2(\phi_2)\right)\\ =\;&-\mu_2\nabla\phi_2+\lambda_2\nabla\left(\frac{\gamma_2^2}{2}|\nabla\phi_2|^2+G_2(\phi_2)\right)+\lambda_1\left(G_1+\frac{\gamma_1^2}{2}|\nabla\phi_1|^2\right)\nabla\phi_2\\ &+\left(\partial_2\lambda_e\frac{1}{2}|\nabla\boldsymbol{\Psi}|^2\right)\nabla\phi_2\end{aligned}$$

with the form of the elastic force term

$$\nabla\cdot\left(\lambda_e(\nabla\boldsymbol{\Psi})^T\nabla\boldsymbol{\Psi}\right)=(\nabla\boldsymbol{\Psi})^T\omega+\frac{\lambda_e}{2}\nabla|\nabla\boldsymbol{\Psi}|^2$$

where $\omega=\nabla\cdot(\lambda_e\nabla\boldsymbol{\Psi})$. This results in the following form of the equation (B.11)

$$\begin{aligned}&\nabla\cdot\left(\lambda_e(\nabla\boldsymbol{\Psi})^T\nabla\boldsymbol{\Psi}\right)+\lambda_2\gamma_2^2\nabla\cdot(\nabla\phi_2\otimes\nabla\phi_2)+\lambda_1\gamma_1^2\nabla\cdot(\phi_2\nabla\phi_1\otimes\nabla\phi_1)\\ =\;&-\mu_1\nabla\phi_1-\mu_2\nabla\phi_2+(\nabla\boldsymbol{\Psi})^T\omega+\nabla\tilde{P}\end{aligned}$$

with

$$\tilde{P}=\left(\lambda_2\frac{\gamma_2^2}{2}|\nabla\phi_2|^2+\lambda_2G_2(\phi_2)+\left(\lambda_1G_1+\frac{\lambda_1\gamma_1^2}{2}|\nabla\phi_1|^2\right)\phi_2+\frac{\lambda_e}{2}|\nabla\boldsymbol{\Psi}|^2\right).$$

Finally, this yields the macroscale momentum equation of the three-phase model

$$\frac{1}{2}[\rho(\partial_t \boldsymbol{u} + \boldsymbol{u}\cdot\nabla\boldsymbol{u}) + (\partial_t(\rho\boldsymbol{u}) + \nabla\cdot(\rho\boldsymbol{u}\otimes\boldsymbol{u}))]$$
$$= \nabla\cdot(\eta\mathbf{D}) - \nabla P - \nabla\mu_1\phi_1 - \nabla\mu_2\phi_2 - (\nabla\boldsymbol{\Psi})^T\omega,$$

where $P = \tilde{P} - \mu_1\phi_1 - \mu_2\phi_2$.

Remark Appendix B.1

Notice that w the variation is taken in the Lagrangian coordinate system when using LAP approach and it is taken in the Eulerian coordinate system in the MDP method. This is done because the variation of the action functional is taken with respect to the flow map (or trajectory $\boldsymbol{x}(\boldsymbol{X},t)$*) and it is more convenient to use the LAP in the Lagrangian coordinates.*

Appendix C. Stability analysis of the numerical scheme

We present in this section the stability analysis of the numerical scheme (3.1). We start by proving the following lemma similar to the one in [29]. This lemma will be used in proving Theorem 3.1.

Lemma Appendix C.1

Let $E = E_c - E_e$*, where* $E_c = \int_\Omega\left(\frac{s_1}{2\varepsilon_1}|\phi_1|^2 + \frac{s_2}{2\varepsilon_2}|\phi_2|^2\right)d\boldsymbol{x}$,

$E_e = \int_\Omega\left(\frac{s_1}{2\varepsilon_1}|\phi_1|^2 + \frac{s_2}{2\varepsilon_2}|\phi_2|^2 - \frac{1}{\varepsilon_2}G_2(\phi_2) - \frac{\phi_2^2}{\varepsilon_1}G_1(\phi_1)\right)d\boldsymbol{x}$*. If*

$s_1 \geq \max\left(G_1''(\phi_1^n)(\phi_2^n)^2, G_1''(\phi_1^n)(\phi_2^n)^2 - 2\phi_2 G_1'(\phi_1^n)\right)$,

$s_2 \geq \max\left(G_2''(\phi_2^n) + \frac{2\varepsilon_2}{\varepsilon_1}G_1, G_2''(\phi_2^n) + \frac{2\varepsilon_2}{\varepsilon_1}(G_1 - \phi_2 G_1'(\phi_1^n))\right)$*, and* $\sup_{\boldsymbol{x}\in\Omega}\{|\phi_1^n|, |\phi_2^n|\} \leq C$ *with a constant* $C > 0$ *then for given* ϕ_1^n *and* ϕ_2^n*, we have*

$$E\left(\phi_1^{n+1}, \phi_2^{n+1}\right) - E(\phi_1^n, \phi_2^n) \leq \left(\bar{\mu}_1^{n+1}, \phi_1^{n+1} - \phi_1^n\right) + \left(\bar{\mu}_2^{n+1}, \phi_2^{n+1} - \phi_2^n\right), \tag{C.1}$$

where $\bar{\mu}_1 = \frac{s_1}{\varepsilon_1}\phi_1^{n+1} - \left(\frac{s_1\phi_1^n}{\varepsilon_1} - (\phi_2^n)^2\frac{G_1'(\phi_1^n)}{\varepsilon_1}\right)$, $\bar{\mu}_2 = \frac{s_2}{\varepsilon_2}\phi_2^{n+1} - \left(\frac{s_2\phi_2^n}{\varepsilon_2} - \frac{G_2'(\phi_2^n)}{\varepsilon_2} - (2\phi_2^n)\frac{G_1(\phi_1^n)}{\varepsilon_1}\right)$.

Proof

By mean value theorem, we have

$$E_c(\phi_1^n, \phi_2^n) - E_c\left(\phi_1^{n+1}, \phi_2^{n+1}\right) \geq \left(\frac{\delta E_c}{\delta\phi_1}, \phi_1^n - \phi_1^{n+1}\right) + \left(\frac{\delta E_c}{\delta\phi_2}, \phi_2^n - \phi_2^{n+1}\right) + \frac{s_1}{\varepsilon_1}|\phi_1^n - \phi_1^{n+1}|^2 + \frac{s_2}{\varepsilon_2}|\phi_2^n - \phi_2^{n+1}|^2. \tag{C.2}$$

Similarly, we can get

$$\begin{aligned} & E_e\left(\phi_1^{n+1},\phi_2^{n+1}\right)-E_e(\phi_1^n,\phi_2^n) \\ = & \left(\frac{\delta E_e(\phi_1^n,\phi_2^n)}{\delta\phi_1},\phi_1^{n+1}-\phi_1^n\right)+\left(\frac{\delta E_e(\phi_1^n,\phi_2^n)}{\delta\phi_2},\phi_2^{n+1}-\phi_2^n\right) \\ & +\left(H_{11},\left(\phi_1^{n+1}-\phi_1^n\right)^2\right)+\left(2H_{12},\left(\phi_1^{n+1}-\phi_1^n\right)\left(\phi_2^{n+1}-\phi_2^n\right)\right) \\ & +\left(H_{22},\left(\phi_2^{n+1}-\phi_2^n\right)^2\right), \end{aligned} \tag{C.3}$$

where

$$\mathbf{H}=\begin{pmatrix} \frac{s_1}{\varepsilon_1}-\frac{\phi_1^2}{\varepsilon_1}G_1''(\phi_1) & -\frac{2\phi_2}{\varepsilon_1'}G_1'(\phi_1) \\ -\frac{2\phi_2}{\varepsilon_1}G_1'(\phi_1) & \frac{s_2}{\varepsilon_2}-\frac{G_2''(\phi_2)}{\varepsilon_2}-\frac{2G_1(\phi_1)}{\varepsilon_1} \end{pmatrix}. \tag{C.4}$$

If $s_1 \geq \max\left(G_1''(\phi_1^n)(\phi_2^n)^2, G_1''(\phi_1^n)(\phi_2^n)^2-2\phi_2 G_1'(\phi_1^n)\right)$,

$s_2 \geq \max\left(G_2''(\phi_2^n)+\frac{2\varepsilon_2}{\varepsilon_1}G_1, G_2''(\phi_2^n)+\frac{2\varepsilon_2}{\varepsilon_1}(G_1-\phi_2 G_1'(\phi_1^n))\right)$, then matrix H is a positive defined matrix.

Then, there exist two constants C_1 and C_2, such that

$$\begin{aligned} & E_e\left(\phi_1^{n+1},\phi_2^{n+1}\right)-E_e(\phi_1^n,\phi_2^n) \\ \geq & \left(\frac{\delta E_e(\phi_1^n,\phi_2^n)}{\delta\phi_1},\phi_1^{n+1}-\phi_1^n\right)+\left(\frac{\delta E_e(\phi_1^n,\phi_2^n)}{\delta\phi_2},\phi_2^{n+1}-\phi_2^n\right) \\ & +C_1|\phi_1^n-\phi_1^{n+1}|^2+C_2|\phi_2^n-\phi_2^{n+1}|^2. \end{aligned} \tag{C.5}$$

Adding (C.2) with (C.5) together gives

$$E\left(\phi_1^{n+1},\phi_2^{n+1}\right)-E(\phi_1^n,\phi_2^n)\leq\left(\bar{\mu}_1^{n+1},\phi_1^{n+1}-\phi_1^n\right)+\left(\bar{\mu}_2^{n+1},\phi_2^{n+1}-\phi_2^n\right).$$

By using above Lemma and multiplying each equation in system (3.1) with proper function, we can prove the energy stable Theorem (3.1) in Section 3.

Theorem 3.1

Let $\mathcal{N}=\max_{\phi_2^n}\left(|\frac{\sqrt{2}}{2}(2\phi_2^n-1)\cos(\theta_s)|\right)$. If s_1 and s_2 satisfy the condition in Lemma Appendix C.1 and $\alpha_w \geq \mathcal{N}$, then the solution $\left(\phi_1^{n+1},\phi_2^{n+1},\boldsymbol{u}^{n+1},P^{n+1},\boldsymbol{\Psi}^{\mathbf{n}+1}\right)$ of the scheme (3.1) satisfies the following discrete energy law for any $\Delta t>0$:

$$
\begin{aligned}
&\mathscr{E}^{n+1} + \frac{(\triangle t)^2}{2\bar{\rho}Re}\|\nabla P^{n+1}\|^2 + \Delta t\left(\frac{1}{2}\|\eta^{1/2}\mathbf{D}(\boldsymbol{u}^{n+1})\|^2\right) \\
&+ \Delta t\left(\|M_1^{1/2}\nabla\mu_1\|^2 + \|M_2^{1/2}\nabla\mu_2\|^2\right) \\
&+ \Delta t\left(\|l_s^{-1/2}\boldsymbol{u}_s^{n+1}\|_w^2 + \kappa\alpha_2\|\dot{\phi}_2^{n+1}\|_w^2\right) \\
\leq\ & \mathscr{E}^n + \frac{(\Delta t)^2}{2\bar{\rho}Re}\|\nabla P^n\|^2
\end{aligned}
\tag{C.6}
$$

Proof of Theorem 3.1

By the definition of λ_e in Section 3, inner product of $\partial_i \lambda_e^{n+1}\frac{|\nabla\boldsymbol{\Psi}^n|^2}{2}$ and $\phi_i^{n+1}-\phi_i^n$, $i=\boldsymbol{1},\boldsymbol{2}$, respectively, and summing them up, result in the following

$$
\begin{aligned}
&\frac{1}{2}\left(\left(\phi_2^{n+1}\right)^2(1-\alpha_{12})\phi_1^{n+1}-\phi_1^n, |\nabla\boldsymbol{\Psi}^n|^2\right) \\
&+\left(\phi_2^{n+1}(\phi_1^n+(1-\phi_1^n)\alpha_{12})\right)\phi_2^{n+1}-\phi_2^n, |\nabla\boldsymbol{\Psi}^n|^2\Big) \\
=\ & \frac{1}{2}\left(\left(\phi_2^{n+1}\right)^2\left(\phi_1^{n+1}+\left(1-\phi_1^{n+1}\right)\alpha_{12}\right), |\nabla\boldsymbol{\Psi}^n|^2\right) \\
&-\frac{1}{2}\left(\left(\phi_2^{n+1}\right)^2(\phi_1^n+(1-\phi_1^n)\alpha_{12}), |\nabla\boldsymbol{\Psi}^n|^2\right) \\
&+\frac{1}{2}\left(\left(\phi_2^{n+1}\right)^2(\phi_1^n+(1-\phi_1^n)\alpha_{12}), |\nabla\boldsymbol{\Psi}^n|^2\right) \\
&-\frac{1}{2}\left(\left(\phi_2^n\right)^2(\phi_1^n+(1-\phi_1^n)\alpha_{12}), |\nabla\boldsymbol{\Psi}^n|^2\right) \\
&+\frac{1}{2}\left(\left(\phi_2^{n+1}-\phi_2^n\right)^2(\phi_1^n+(1-\phi_1^n)\alpha_{12}), |\nabla\boldsymbol{\Psi}^n|^2\right) \\
=\ & \frac{1}{2}\left\|\left(\lambda_e^{n+1}\right)^{1/2}\nabla\boldsymbol{\Psi}^n\right\|^2-\frac{1}{2}\left\|\left(\lambda_e^n\right)^{1/2}\nabla\boldsymbol{\Psi}^n\right\|^2 \\
&+\frac{1}{2}\left(\left(\phi_2^{n+1}-\phi_2^n\right)^2(\phi_1^n+(1-\phi_1^n)\alpha_{12}), |\nabla\boldsymbol{\Psi}^n|^2\right)
\end{aligned}
\tag{C.7}
$$

And for the hydrophilic term, inner product of $\nabla\cdot\left(\left(\phi_2^{n+1}\right)^2\nabla\phi_1^{n+1}\right)$ and $\phi_2^{n+1}|\nabla\phi_1^n|^2$ by $\phi_1^{n+1}-\phi_1^n$ and $\phi_2^{n+1}-\phi_2^n$, respectively, and summing them up have the form

$$
\begin{aligned}
&-\varepsilon_1\left(\nabla\cdot\left(\left(\phi_2^{n+1}\right)^2\nabla\phi_1^{n+1}\right), \phi_1^{n+1}-\phi_1^n\right)+\varepsilon_1\left(\phi_2^{n+1}|\nabla\phi_1^n|^2, \phi_2^{n+1}-\phi_2^n\right) \\
=\ & \varepsilon_1\left(\left(\phi_2^{n+1}\right)^2\nabla\phi_1^{n+1}, \nabla\phi_1^{n+1}-\nabla\phi_1^n\right)+\varepsilon_1\left(|\nabla\phi_1^n|^2\phi_2^{n+1}, \phi_2^{n+1}-\phi_2^n\right) \\
=\ & \frac{\varepsilon_1}{2}\left(\left(\phi_2^{n+1}\right)^2, |\nabla\phi_1^{n+1}|^2-|\nabla\phi_1^n|^2+|\nabla\left(\phi_1^{n+1}-\nabla\phi_1^n\right)|^2\right) \\
&+\frac{\varepsilon_1}{2}\left(|\nabla\phi_1^n|^2, \left(\phi_2^{n+1}\right)^2-\left(\phi_2^n\right)^2+\left(\phi_2^{n+1}-\phi_2^n\right)^2\right) \\
=\ & \frac{\varepsilon_1}{2}\left\|\phi_2^{n+1}\nabla\phi_1^{n+1}\right\|^2-\frac{\varepsilon_1}{2}\|\phi_2^n\nabla\phi_1^n\|^2 \\
&+\frac{\varepsilon_1}{2}\left\|\left(\phi_2^{n+1}\right)\nabla\left(\phi_1^{n+1}-\phi_1^n\right)\right\|^2+\frac{\varepsilon_1}{2}\left\|\left(\phi_2^{n+1}-\phi_2^n\right)\nabla\phi_1^n\right\|^2.
\end{aligned}
\tag{C.8}
$$

Combining equations (C.7)–(C.8) and Lemma Appendix C.1, results in the following inequality

$$\begin{aligned} & \mathscr{E}_{coh}^{n+1} + \mathscr{E}_{w}^{n+1} - \left(\mathscr{E}_{coh}^{n} + \mathscr{E}_{w}^{n}\right) \\ & + \frac{\alpha_e}{2}\left(\left\|\left(\lambda_e^{n+1}\right)^{1/2}\nabla\Psi^n\right\|^2 - \left\|\left(\lambda_e^{n}\right)^{1/2}\nabla\Psi^n\right\|^2\right) \\ \leq\ & \left(\mu_1^{n+1}, \phi_1^{n+1} - \phi_1^{n}\right) + \left(\mu_2^{n+1}, \phi_2^{n+1} - \phi_2^{n}\right) \\ & + \alpha_2\left(L\left(\phi_2^{n+1}\right), \phi_2^{n+1} - \phi_2^{n}\right)w\,. \end{aligned} \tag{C.9}$$

After taking the inner product of the first and second equations in (3.1a) with $\Delta t\mu_1^{n+1}$ and $\Delta t\mu_2^{n+1}$, respectively, we have

$$\left(\phi_1^{n+1} - \phi_1^{n}, \mu_1^{n+1}\right) - \Delta t\left(\boldsymbol{u}^{n+1}\phi_1^{n+1}, \nabla\mu_1^{n+1}\right) + \triangle t M_1\left\|\nabla\mu_1^{n+1}\right\|^2 = 0, \tag{C.10}$$

$$\left(\phi_2^{n+1} - \phi_2^{n}, \mu_2^{n+1}\right) - \Delta t\left(\boldsymbol{u}^{n+1}\phi_2^{n+1}, \nabla\mu_2^{n+1}\right) + \Delta t M_2\left\|\nabla\mu_2^{n+1}\right\|^2 = 0. \tag{C.11}$$

Taking the inner product of the first equation in (3.1b) with $\Delta t\boldsymbol{u}^{n+1}$ yields

$$Re\left(\frac{\rho^{n+1}\boldsymbol{u}^{n+1} - \rho^{n}\boldsymbol{u}^{n}}{2\Delta t} + \frac{\rho^{n}\left(\boldsymbol{u}^{n+1} - \boldsymbol{u}^{n}\right)}{2\Delta t}, \boldsymbol{u}^{n+1}\right) \tag{C.12}$$

$$= \mathrm{Re}\left(\frac{1}{2}\left(\rho^{n+1} + \rho^{n}\right)\mathbf{u}^{n+1} - \rho^{n}\mathbf{u}^{n}, \mathbf{u}^{n+1}\right) \tag{C.13}$$

$$= \frac{Re}{2}\left(\left\|\zeta^{n+1}\boldsymbol{u}^{n+1}\right\|^2 - \left\|\zeta^{n}\boldsymbol{u}^{n}\right\|^2 + \left\|\zeta^{n}\left(\boldsymbol{u}^{n+1} - \boldsymbol{u}^{n}\right)\right\|^2\right) \tag{C.14}$$

$$\begin{aligned} = \ & -\frac{\Delta t}{2}\left\|\left(\eta\left(\phi^{n+1}\right)\right)^{1/2}\mathbf{D}\left(\boldsymbol{u}^{n+1}\right)\right\|^2 + \Delta t\left(\nabla\left(-2P^{n} + P^{n-1}\right), \boldsymbol{u}^{n+1}\right) \\ & - \Delta t\left(\phi_1^{n+1}\nabla\mu_1^{n+1}, \boldsymbol{u}^{n+1}\right) - \triangle t\left(\phi_2^{n+1}\nabla\mu_2^{n+1}, \boldsymbol{u}^{n+1}\right) \\ & - \alpha_e\Delta t\left(\left(\nabla\Psi^{n}\right)^{T}\omega^{n+1}, \boldsymbol{u}^{n+1}\right) + \Delta t\left(\eta\left(\phi^{n+1}\right)\boldsymbol{\tau}\cdot\mathbf{D}\left(\phi^{n+1}\right)\cdot n, \boldsymbol{u}_s^{n+1}\right)_w, \end{aligned}$$

where $\omega^{n+1} = \nabla\cdot\left(\lambda_e^{n+1}\nabla\boldsymbol{\Psi}^{n+1}\right)$. Here we use the fact that $\int_\Omega\left(\nabla\cdot\left(\rho^{n+1}\boldsymbol{u}^{n+1}\otimes\boldsymbol{u}^{n}\right) + \rho^{n+1}\boldsymbol{u}^{n}\cdot\nabla\boldsymbol{u}^{n+1}, \boldsymbol{u}^{n+1}\right)d\boldsymbol{x} = 0$.

By using the same argument as in [29], the pressure can be estimated as follows

$$\begin{aligned} & \Delta t\left(\boldsymbol{u}^{n+1}, \nabla\left(-2P^{n+1}+P^{n}\right)\right) \\ \leq\ & \frac{(\Delta t)^{2}}{2\bar{\rho}Re}\left(-\left\|\nabla\left(P^{n}-P^{n-1}\right)\right\|^{2}-\|\nabla P^{n+1}\|^{2}+\|\nabla P^{n}\|^{2}\right) \\ & +\frac{Re}{2}\left\|\zeta^{n}\left(\boldsymbol{u}^{n+1}-\boldsymbol{u}^{n}\right)\right\|^{2}. \end{aligned} \tag{C.15}$$

Taking gradient of each component of the third equation in (3.1b), yields

$$\frac{\partial_j \boldsymbol{\Psi}_i^{n+1}-\partial_j \boldsymbol{\Psi}_i^{n}}{\triangle t}+\partial_j\left(\boldsymbol{u}_k^{n+1}\partial_k \boldsymbol{\Psi}_i^{n}\right)=0. \tag{C.16}$$

The inner product of above equation with $\alpha_e \Delta t \lambda_e^{n+1}\partial_k \boldsymbol{\Psi}_i^{n+1}$ results in

$$\begin{aligned} & \frac{\alpha_e}{2}\left(\left\|\left(\lambda_e^{n+1}\right)^{1/2}\boldsymbol{\Psi}^{n+1}\right\|^{2}-\left\|\left(\lambda_e^{n+1}\right)^{1/2}\boldsymbol{\Psi}^{n}\right\|^{2}\right) \\ \leq\ & \alpha_e \Delta t\left(\left(\nabla \boldsymbol{\Psi}^{n}\right)^{T}\omega^{n+1}, \boldsymbol{u}^{n+1}\right) \\ & -\alpha_e\left(\tau\cdot\left(\phi_2^{n+1}\right)^{2}\left(\nabla \boldsymbol{\Psi}^{n}\right)^{T}\nabla \boldsymbol{\Psi}^{n+1}\cdot n, \boldsymbol{u}_s^{n+1}\right)_w. \end{aligned} \tag{C.17}$$

Adding equation (C.12) to the equation (C.17) yields

$$\begin{aligned} & \frac{Re}{2}\left(\left\|\zeta^{n+1}\boldsymbol{u}^{n+1}\right\|^{2}-\left\|\zeta^{n}\boldsymbol{u}^{n}\right\|^{2}+\left\|\zeta^{n}\left(\boldsymbol{u}^{n+1}-\boldsymbol{u}^{n}\right)\right\|^{2}\right) \\ & +\frac{\alpha_e}{2}\left(\left\|\left(\lambda_e^{n+1}\right)^{1/2}\boldsymbol{\Psi}^{n+1}\right\|^{2}-\left\|\left(\lambda_e^{n+1}\right)^{1/2}\boldsymbol{\Psi}^{n}\right\|^{2}\right. \\ \leq\ & -\frac{\Delta t}{2}\left\|\left(\eta\left(\phi^{n+1}\right)\right)^{1/2}\mathbf{D}\left(\boldsymbol{u}^{n+1}\right)\right\|^{2}+\Delta t\left(\nabla\left(-2P^{n}+P^{n-1}\right), \boldsymbol{u}^{n+1}\right) \\ & -\Delta t\left(\phi_1^{n+1}\nabla \mu_1^{n+1}, \boldsymbol{u}^{n+1}\right)-\triangle t\left(\phi_2^{n+1}\nabla \mu_2^{n+1}, \boldsymbol{u}^{n+1}\right) \\ & -\left\|l_s^{1/2}\mathbf{u}_s^{n+1}\right\|_w^2+\alpha_2\left(L\left(\phi_2^{n+1}\right)\partial_\tau \phi_2^{n+1}, \boldsymbol{u}_s^{n+1}\right)_w. \end{aligned} \tag{C.18}$$

Combing equations (C.9)–(C.11), (C.18) with pressure estimation (C.15) results in the equation (3.2). ■

Appendix D. Additional Simulation Figures

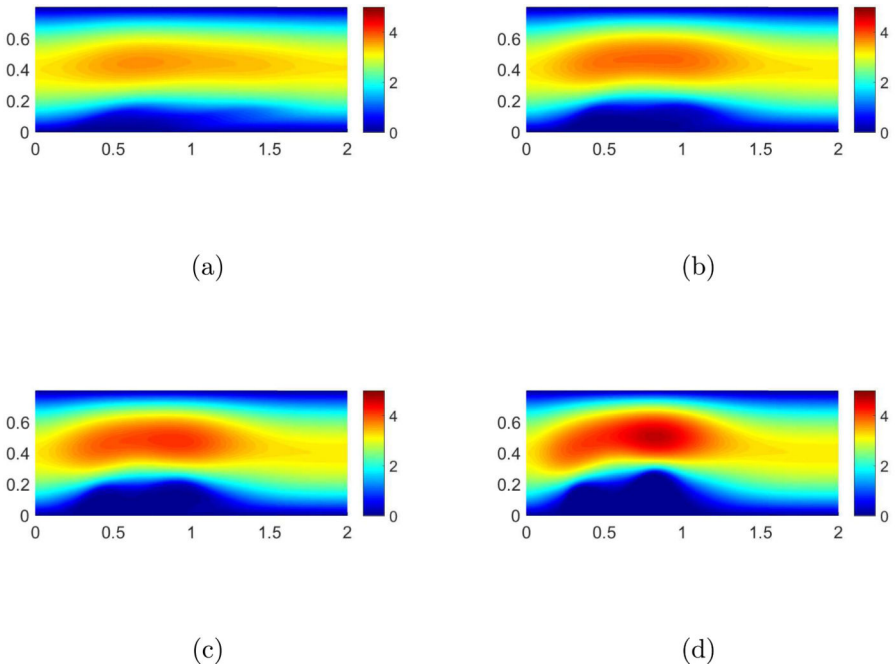

Figure D.11:

Profiles of velocity norm at steady state with different values of elasticity for fibrin network and platelet aggregate. (a) $\lambda_n = 0.1Pa$, $\lambda_p = 1Pa$. (b) $\lambda_n = 1Pa$, $\lambda_p = 10Pa$. (c) $\lambda_n = 10Pa$, $\lambda_p = 10Pa$. (d) $\lambda_n = 50Pa$, $\lambda_p = 10Pa$.

References

[1]. Abels H, Garcke H, Grün G, Thermodynamically consistent, frame indifferent diffuse interface models for incompressible two-phase flows with different densities, Math. Models Methods Appl. Sci 22(3), 1150013, 2012.

[2]. Abedijaberi A, Bhatara G, Shaqfeh ESG, Khomami B, A computational study of the influence of visco-elasticity on the interfacial dynamics of dip coating flow, J. Non-Newtonian Fluid Mech 166, 614–627, 2011.

[3]. Anderson DM, McFadden GB, Wheeler AA, Diffusive-interface methods in fluid dynamics, Annu. Rev. Fluid. Mech 30 139–165, 1998.

[4]. Arnold VI, Mathematical methods of classical mechanics, second edition, Springer-Verlag, New York, 1989.

[5]. Badalassi VE, Ceniceros HD, Banerjee S, Computation of multi-phase systems with phase field models, J. Comput. Phys 190, 371–397, 2003.

[6]. Bajd F, Sersa I, Mathematical Modeling of Blood Clot Fragmentation During Flow-Mediated, Thrombosis, Biophys. J 104: 1181–90, 2013; [PubMed: 23473501]

[7]. Bajaj M, Prakash JR, Pasquali M, A computational study of the effect of visco-elasticity on slot coating flow of dilute polymer solutions, J. Non-Newtonian Fluid Mech 149, 104–123, 2008.

[8]. Bell JB, Marcus DL, A second-order projection method for variable-density flows, J. Comput. Phys 101, 334–348, 1992.

[9]. Bird RB, Armstrong RC, Hassafer O, Dynamics of polymeric fluids, 1, New York, NY: Wiley.

[10]. Borkar AV, Tsamopoulos JA, Gupta SA, Gupta RK, Spin coating of visco-elastic and nonvolatile fluids over a planar disk, Phys. Fluids 6, 3539–3553, 2007.

[11]. Boyer F, Lapuerta C, Study of a three component Cahn-Hilliard flow model, Math. Model. Numer. Anal 40, 653–687,2006.

[12]. Brannick J, Liu C, Qian T, Sun H, Diffuse Interface Methods for Multiple Phase Materials: An Energetic Variational Approach, Numer. Math. Theor. Meth. Appl 8, 220–236,2014.

[13]. Cahn JW, Hilliard JE, Free energy of a nonuniform system. I. Interface free energy, J. Chem. Phys 28, 258–267, 1958.

[14]. A Campbell R, Overmyer KA, Bagnell CR, Wolberg AS, Cellular procoagulant activity dictates clot structure and stability as a function of distance from the cell surface, Arterioscler Thromb. Vase. Biol 28(12), 2247–2254, 2008.

[15]. Chorin AJ, Numerical solution of the Navier-Stokes equations, Math. Comput 22, 745–762, 1968.

[16]. Dandapat BS, Singh SK, Cell Movement Is Guided by the Rigidity of the Substrate, Biophys. J 79, 1,Volume 79, 144–152, 2000. [PubMed: 10866943]

[17]. Di Y, Li R, Tang T, A general moving mesh framework in 3D and its application for simulating the mixture of multi-phase flows, Commun. Comput. Phys 3, 582–602, 2008.

[18]. Ding H, Spelt PDM, and Shu C, Diffuse interface model for incompressible two-phase flows with large density ratios, J. Comput. Phys 226, 2078–2795, 2007.

[19]. Ding H, Spelt PDM, Wetting condition in diffuse interface simulations of contact line motion, Phys. Rev. E 75, 046708, 2007.

[20]. Dong S, An efficient algorithm for incompressible N-phase flows, J. Comput. Phys 276, 691–728, 2014.

[21]. Eisenberg B, Hyon Y, Chun Liu, Energy variational analysis of ions in water and channels: Field theory for primitive models of complex ionic fluids, J. Chem. Phys 133(10), 104104, 2010. [PubMed: 20849161]

[22]. Eyre DJ, An unconditionally stable one-step scheme for gradient systems, Unpublished article, 6 1998.

[23]. Eyre DJ, in Bullard JW et al. (Eds.), Computational and mathematical models of microstructural evolution, The Materials Research Society, Warrendale, PA, 39–46, 1998.

[24]. Feng X, Tang T, Yang J, Long time numerical simulations for phase-field problems using p-adaptive spectral deferred correction methods, SIAM J. Sci. Comput 37(1), 271–294, 2014.

[25]. Fontelos M, Grün G, Jörres S, On a Phase-Field Model for Electrowetting and Other Electrokinetic Phenomena, SIAM J. Math. Anal 43, 527–563, 2011

[26]. Forster Johannes, Mathematical Modeling of Complex Fluids, master theis, University of Wüurzburg, 2013.

[27]. Galdi GP, Rannacher R, Robertson AM and Turek S, Hemodynamical flows Modeling, Analysis and Simulation, 37, Birkhäuser Basel, 2008.

[28]. Gao M, Wang X-P, A gradient stable scheme for a phase field model for the moving contact line problem, J. Comput. Phys 231, 1372–1386, 2012.

[29]. Gao M, Wang X-P, An efficient scheme for a phase field model for the moving contact line problem with variable density and viscosity, J. Comput. Phys 272, 704–718, 2014.

[30]. Garcke H, Hinze M, Kahle C, A stable and linear time discretization for a thermodynamically consistent model for two-phase incompressible ow, Applied Numerical Mathematics, 99, 151–171, 2016.

[31]. Gersh KC, Nagaswami C, Weisel JW, Fibrin network structure and clot mechanical properties are altered by incorporation of erythrocytes, Thromb Haemost. 102(6), 1169–75, 2009. [PubMed: 19967148]

[32]. Guermond J-L, Salgado A, A splitting method for incompressible flows with variable density based on a pressure Poisson equation, J. Comput. Phys 228, 2834–2846, 2009.

[33]. Guermond J-L, Quartapelle L, A projection FEM for variable density incompressible flows, J. Comput. Phys 165(1), 167–188, 2000.

[34]. Guo Z, Lin P, A thermodynamically consistent phase-field model for two-phase flows with thermocapillary effects, J. Fluid Mech 766, 226771, 2015.

[35]. He Y, Liu Y, Tang T, On large time-stepping methods for the Cahn-Hilliard equation, Appl. Numer. Math 57, 616–628, 2007.

[36]. Heemskerk JW, Bevers EM, Lindhout T, Platelet activation and blood coagulation, Thromb. Haemost. 88(2), 186–93, 2002. [PubMed: 12195687]

[37]. Hohenberg PC and Halperin BI, Theory of dynamic critical phenomena, Rev. Mod. Phys 49, 435–479, 1977

[38]. Huang C-C, Chen P-Y, Shih C-C, Estimating the viscoelastic modulus of a thrombus using an ultrasonic shear-wave approach, Med. Phys 40(4),042901, 2013 [PubMed: 23556923]

[39]. Hyon Y, Kwak DY, Liu C, Energetic variational approach in complex fluids: maximum dissipation principle, DCDS-A 24(4), 1291–1304, 2010.

[40]. Jacqmin D, Contact-line dynamics of a diffuse fluid interface, J. Fluid Mech 402, 57–88, 2000.

[41]. Jiang J, Li Y, Liu C, Two-phase Incompressible Flows with Variable Density: An Energetic Variational Approach, DCDS-A 37(6), 2017.

[42]. Van Kempen THS, Bogaerds ACB, Peters GWM, van de Vosse FN, A Constitutive Model for a Maturing Fibrin Network, Biophys. J 107(2), 504–513, 2014. [PubMed: 25028892]

[43]. Kim E, Kim OV, Machlus KR, Liu X, Kupaev T, Lioi J, Wolberg AS, Chen DZ, Rosen ED, Xu Z, Alber M, Correlation between fibrin network structure and mechanical properties: an experimental and computational analysis, Soft Matter 7, 4983–4992, 2011.

[44]. Kim JS, Kang KK, Lowengrub JS, Conservative multigrid methods for Cahn- Hilliard fluids, J. Comput. Phys 193, 511–543, 2004.

[45]. Kim JS, Kang KK, Lowengrub JS, Conservative multigrid methods for ternary Cahn- Hilliard systems, Comm. Math. Sci 2, 53–77, 2004.

[46]. Kim JS, Lowengrub JS, Phase field modeling and simulation of three-phase flows, Int. Free Bound 7, 435–466, 2005.

[47]. Kim JS, Phase-field models for multi-component fluid flows, Commun. Comput. Phys 12(3), 613–661, 2012.

[48]. Kim OV, Xu Z, Rosen ED, Albe M, Fibrin networks regulate protein transport during thrombus Development, PLoS Comput. Biol 9(6): e1003095, 2013. [PubMed: 23785270]

[49]. Lin FH, Liu C, Zhang P, On hydrodynamcis of visco-elastic fluids, Commum. Pure Appl. Math 58, 1437–1471, 2005.

[50]. Liu C, Shen J, Yang XF, Decoupled energy stable schemes for a phase-field model of two-phase incompressible flows with variable density, J. Sci. Comput 62(2), 601–622, 2015.

[51]. Liu C, Shen J, A phase field model for the mixture of two incompressible fluids and its approximation by a Fourier-spectral method, Physica D 179, 211–228, 2003.

[52]. Lowengrub J, Truskinovsky L, Quasiincompressible CahnHilliard fluids and topological transitions, Proc. R. Soc. Lond. A 454, 2617–2654, 1998;

[53]. Onsager L, Reciprocal relations in irreversible processes. L, Phys. Rev. II. Ser 37, 405–426, 1931.

[54]. Onsager L, Reciprocal relations in irreversible processes. IL, Phys. Rev. II. Ser 38, 2265–2279, 1931.

[55]. Ovanesov MV, Krasotkina JV, Ul'yanova LI et al., Hemophilia A and B are associated with abnormal spatial dynamics of clot growth. Biochim. Biophys. Acta 1572(1), 45–57, 2002. [PubMed: 12204332]

[56]. zkaya N, Fundamentals of Biomechanics : Equilibrium, Motion, and Deformation. New York : Springer Verlag, 2012.

[57]. Polanowska-Grabowska R, Raha S, Gear AR, Adhesion efficiency, platelet density and size, Br. J. Haematol 82, 715–720, 1992. [PubMed: 1282829]

[58]. Qian T, Wang X-P, Sheng P, Molecular scale contact line hydrodynamics of immiscible flows, Phys. Rev. E 68, 016306, 2003.

[59]. Qian T, Wang X-P, Sheng P, Molecular hydrodynamics of the moving contact line in two-phase immiscible flows, Commun. Comput. Phys 1, 1–52, 2006.

[60]. Qian T, Wang X-P, Sheng P, A variational approach to the moving contact line hydrodynamics, J. Fluid Mech 564, 333–360, 2006.

[61]. Rafaï S, Bonn D, and Boudaoud A, Spreading of non-Newtonian fluids on hydrophilic surfaces, J. FluidMech 513, 77, 2004.

[62]. Ranucci M, Laddomada T, Ranucci M, and Baryshnikova E, Blood viscosity during coagulation at different shear rates, Physiological Reports, 2(7), 2014.

[63]. Ren W, W. E, Boundary conditions for the moving contact line problem, Phys. Fluids 10, 022101, 2007.

[64]. Ren W, Hu D, W. E, Continuum models for the contact line problem, Phys. Fluids 22, 102103, 2010.

[65]. Della Rocca G, Blanquart G, Level set reinitialization at a contact line, J. Comput. Phys 265 (2014) 34–49.

[66]. Ryham RJ, An energetic variational approach to mathematical modeling of charged fluids: charge phases,simulation and well posednes, thesis Pennsylvania State University, 2006.

[67]. Shen J, Wang C, Wang XM, Wise SM, Second-order convex splitting schemes for gradient flows with Ehrlich-Schwoebel type energy: Application to thin film epitaxy, SIAM J. Numer. Anal 50(1), 105–125, 2012.

[68]. Shen J, Yang X, A phase-field model and its numerical approximation for two-phase incompressible flows with different densities and viscosities, SIAM, J. Sci. Comput 32(3), 1159–1179, 2010.

[69]. Shen J, Yang X, Numerical approximations of Allen-Cahn and Cahn-Hilliard equations, DCDS-A 28(4), 1669–1691, 2010.

[70]. Stalker TJ, Welsh JD, Tomaiuolo M, Wu J, Colace TV, Diamond SL, and Brass LF, A systems approach to hemostasis: 3. Thrombus consolidation regulates intrathrombus solute transport and local thrombin activity, Blood. 124(11), 1824–31, 2014. [PubMed: 24951426]

[71]. Stalker TJ, Traxler EA, Wu J, Wannemacher KM, Cermignano SL, Voronov R, Diamond SL, and Brass LF, Hierarchical organization in the hemostatic response and its relationship to the platelet-signaling network, Blood. 121(10), 1875–85, 2013. [PubMed: 23303817]

[72]. Temam R, Sur l'approximation de la solution des équations de Navier-Stokes par la méthode des pas fractionnaires II, Arch. Rat. Mech. Anal 33, 377–385, 1969.

[73]. Tierra G, Pavissich JP, Nerenberg R, Xu Z, Alber M, Multicomponent model of deformation and detachment of a biofilm under fluid flow, J. R. Soc. Interface 12, 20150045, 2015. [PubMed: 25808342]

[74]. Trudnowski RJ, Rico RC, Specific gravity of blood and plasma at 4 and 37 degrees C, Clin. Chem 20, 615–616, 1974. [PubMed: 4826961]

[75]. Undas A, Ariëns RA, Fibrin clot structure and function: a role in the pathophysiology of arterial and venous thromboembolic diseases, Arterioscler Thromb. Vase. Biol 31(12), 88–99, 2011.

[76]. Walker SW, A Mixed Formulation of A Sharp Interface Model Of Stokes Flow With Moving Contact Lines ESAIM: Mathematical Modelling and Numerical Analysis, 48, 969–1009, 2014

[77]. Wang Y, Minh D-Q, Amberg G, Dynamic wetting of viscoelastic droplets, Phys. Rev. E, 92, 043002, 2015.

[78]. Welsh JD, Stalker TJ, Voronov R, Muthard RW, Tomaiuolo M, Diamond SL, Brass LF, A systems approach to hemostasis: 1. The interdependence of thrombus architecture and agonist movements in the gaps between platelets, Blood 124(11), 1808–15, 2014. [PubMed: 24951424]

[79]. Wu S, Xu J, Multiphase AllenCahn and CahnHilliard models and their discretizations with the effect of pairwise surface tensions, Journal of Computational Physics 343 (15), 10–32 2017.

[80]. Xu S, Ren W, Reinitialization of the level set function in 3d simulation of moving contact lines, Commun. Comput. Phys 20(5), 1163–1182, 2016.

[81]. Xu Z, Chen N, Kamocka MM, Rosen ED, Alber M, A multiscale model of thrombus development, J. R. Soc. Interface 5(24), 705–22, 2008. [PubMed: 17925274]

[82]. Xu ZL, Lioi J, Mu J, Kamocka MM, Liu X, Chen DZ, Rosen ED, Alber M, A multiscale model of venous thrombus formation with surface-mediated control of blood coagulation cascade, Biophyical J. 98, 1723–1732, 2010.

[83]. Xu S, Sheng P, Liu C, An energetic variational approach for ion transport, Commun. Math. Sci 12(4), 779–789, 2014.

[84]. Yue P, Feng JJ, Wall energy relaxtion in the Cahn-Hilliard model for moving contact lines, Phys. Fluids 23, 012106, 2011.

[85]. Yue P, Feng JJ, Phase-field simulations of dynamic wetting of visco-elastic fluids, J. Non-Newton. Fluid 189-190, 8–13, 2012.

[86]. Yue P, Feng JJ, Chun Liu J Shen, A diffuse-interface method for simulation two-phase flows of complex fluids, J. Fluid Mech 515, 293–317, 2004.

[87]. Yue P, Zhou C, Feng JJ, Sharp-interface limit of the Cahn-Hilliard model for moving contact lines, J. Fluid Mech 645, 279–294, 2010.

[88]. Zhang Q, Wang X-P, Phase field modeling and simulation of three phase flow on solid surface, J. Comput. Phys 319, 79–107, 2016.

[89]. Zhang TY, Cogan N, Wang Q, Phase Field Models for Biofilms. I. Theory and 1-D simulations, SIAM J. Appl. Math 69 (3), 641–669, 2008.

[90]. Zhou C, Yue P, Feng JJ, Ollivier-Gooch CF, Hu HH, 3D phase-field simulations of interfacial dynamics in Newtonian and visco-elastic fluids, J. Comput. Phys 229, 498–511, 2010.

[91]. Zucker MB, Nachmias VT, Platelet activation, Arterioscler Thromb Vase Biol. 5, 2–18, 1985.

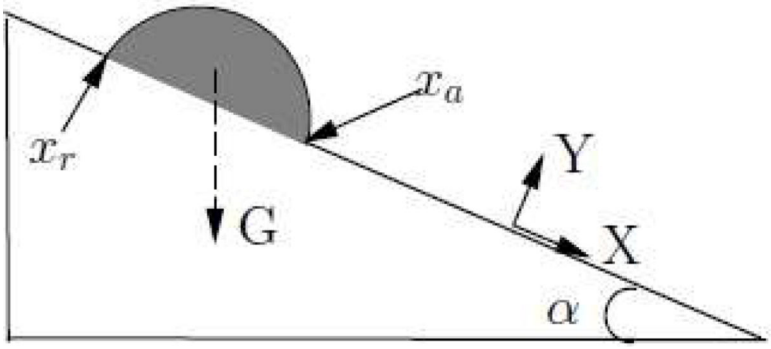

Figure 1:
Diagram of the droplet sliding on an inclined plane under gravitational force.

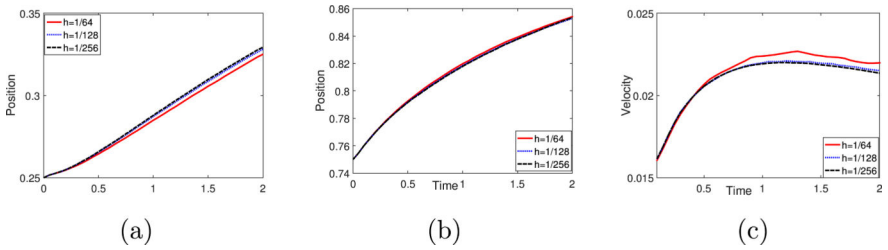

Figure 2:

Convergence study of the numerical scheme by simulating droplet sliding on an inclined plane, (a) Motion of the receding contact point x_r by using different meshes, (b) Motion of the advancing contact point x_a with different meshes, (c) Velocity of the receding contact point x_r by using different meshes.

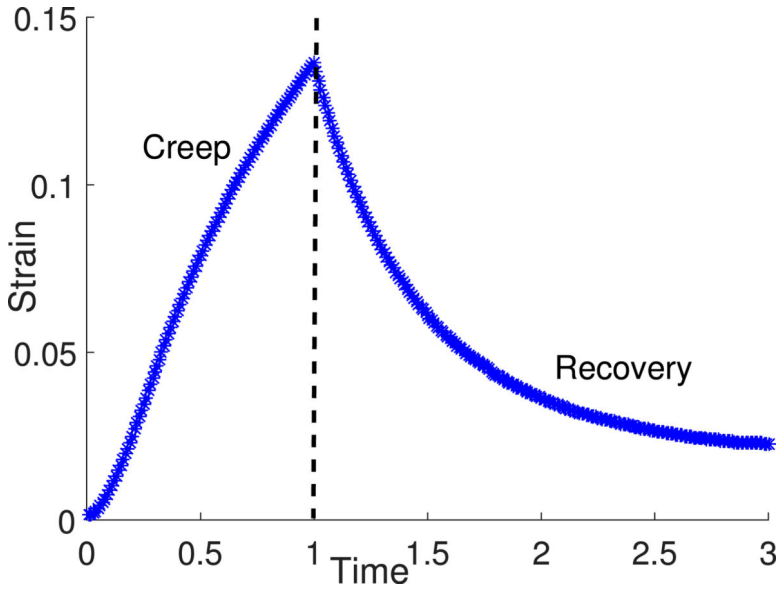

Figure 3:

Creep and Recovery. The inlet flow velocity specified by $u = 20(0.5 - y)y$ is added until $t = 1$ on the left boundary of the domain. Then the inlet flow velocity is set to be zero.

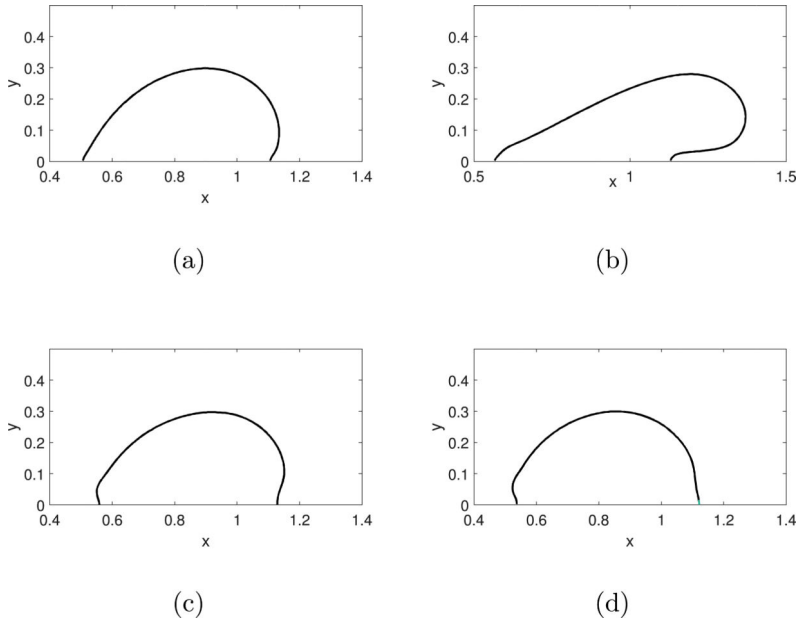

Figure 4:

Interface of the droplet at time (a) $t = 0.1$, (b) $t = 1$, (c) $t = 2$, and (d) $t = 3$ for creep-recovery test. The Kelvin-Voigt model is used for describing droplet visco-elasticity.

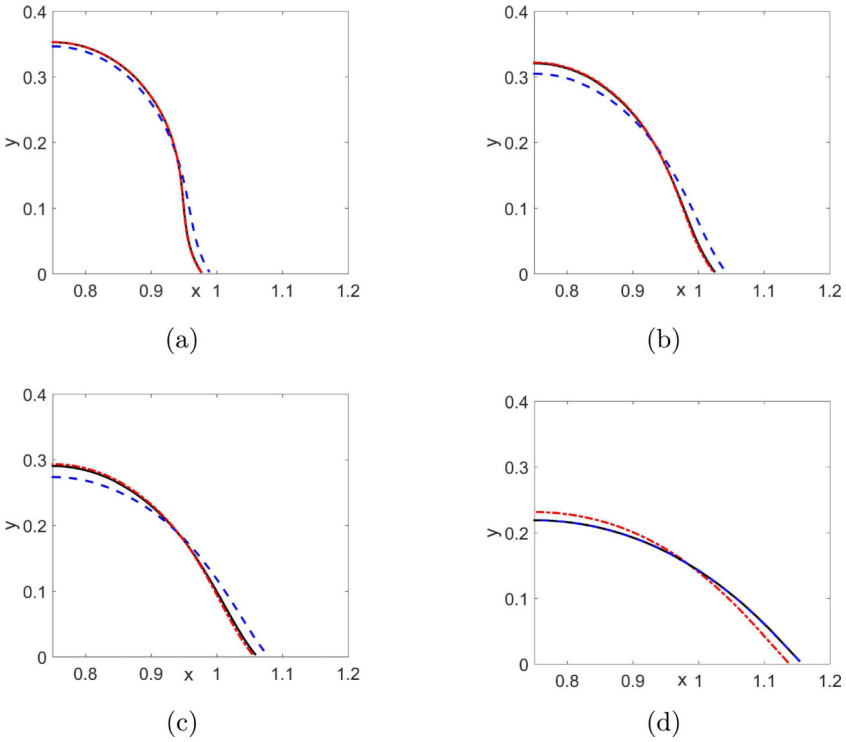

Figure 5:

Spontaneous plot of interface profiles of the simulated droplets when they spread on the plane. Due to symmetry, only parts of the interfaces in $x > 0$ plane are plotted. (a) $t = 0.5$; (b) $t = 1$; (c) $t = 1.5$; and (d) $t = 5$. Black line: Pure Newtonian droplet. Blue dash line: Droplet with the Oldroyd-B model. Red dash dot line: Droplet with the Kelvin-Voigt model.

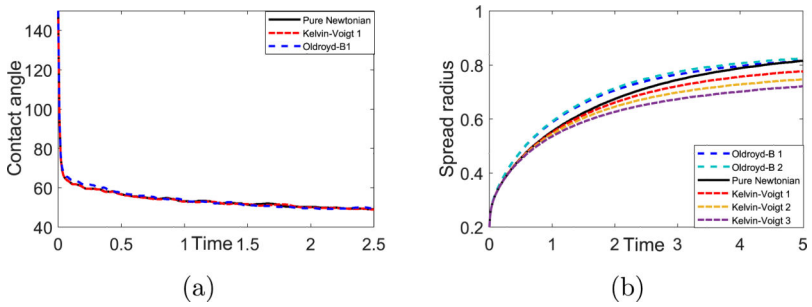

Figure 6:

(a) Contact angles and (b) radius of simulated spreading droplets. Black line corresponds to the pure Newtonian droplet. Red, brown and purple dash dot lines correspond to the Kelvin-Voigt type visco-elastic droplet with different shear modulus, a_e = 2, 5, 10, respectively. Blue and green dash lines indicate data for the Oldroyd-B visco-elastic droplets with different relaxation times W_i = 2, 5, respectively.

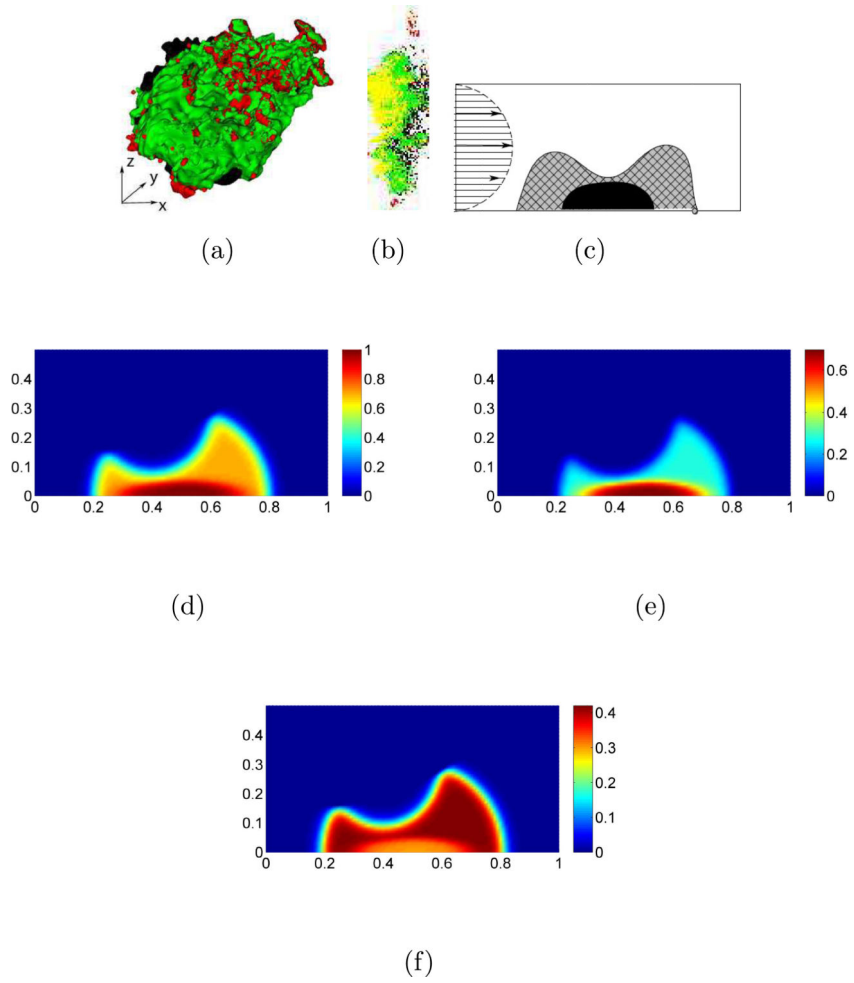

Figure 7:

Initial structure of the blood clot in a vein, (a) Reconstructed three-dimensional image of a venule blood clot from *in vivo* experiments in mice. (Original image was published in [43, 82].) Platelets are indicated in red, fibrin is in green, yellow indicates combination of platelets and fibrin, and black is used for other blood cells. Images show that platelet aggregate in the middle of the clot is covered by the fibrin network and that the surface of the blood clot consists mainly of the fiber network, (b) *yz* cross section of the reconstructed image of the blood clot; (c) Schematic diagram of the clot structure used in simulations of a blood clot deformation under shear flow. Blood flow enters on the left side of the simulation domain with a parabolic profile and exits on the right side of the domain, (d) Initial distribution of the volume fraction of the blood clot represented by the phase function $\phi_2(t = 0)$. (e) Initial distribution of the volume fraction of platelets represented by $\phi_1(t = 0)$. (f) Initial distribution of the volume fraction of the fibrin network represented by $(1 - \phi_1(t = 0))$.

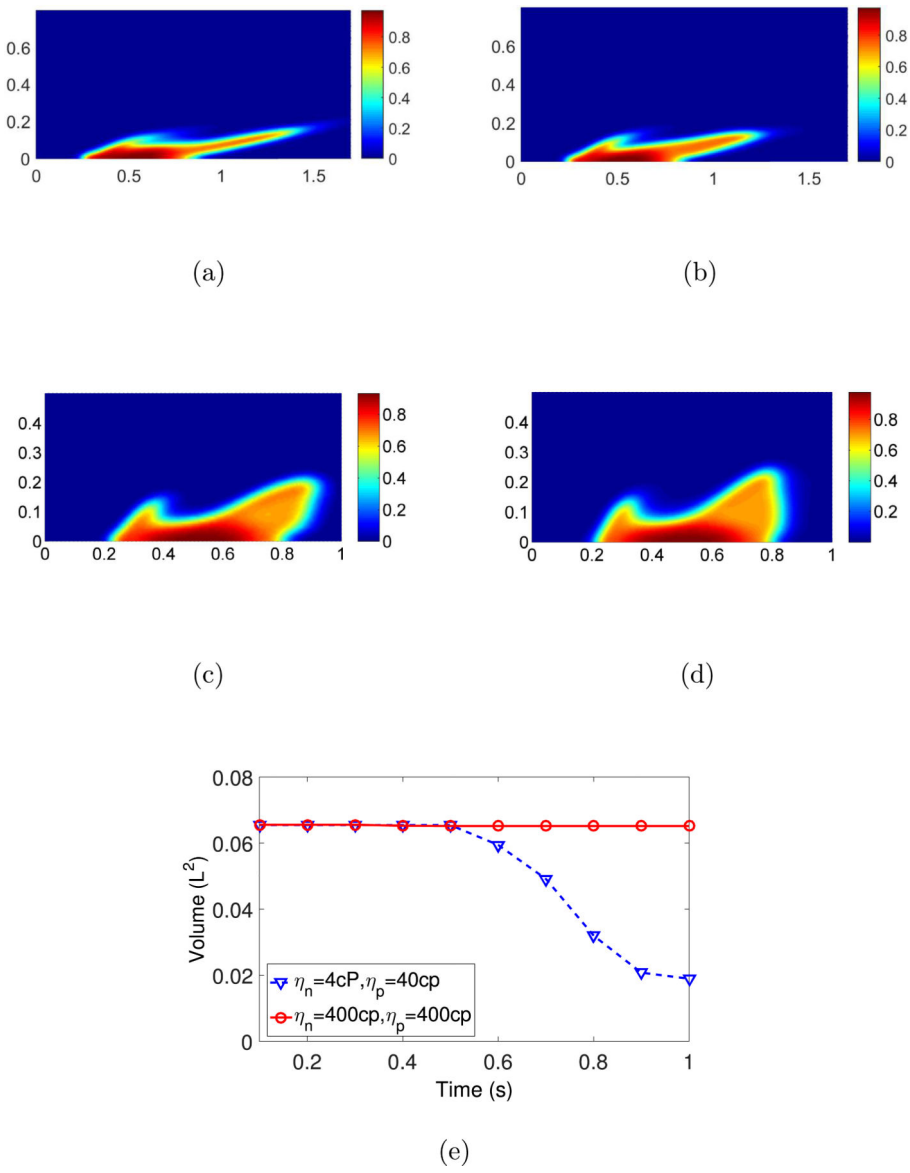

Figure 8:

Shapes of clots with different values of viscosity described by steady state solutions of the model system of equations with fixed elasticity modulus $\lambda_n = 1Pa$, $\lambda_p = 10Pa$. (a) $\eta_n = 4cP$, $\eta_p = 40cP$, (b) $\eta_n = 40cP$, $\eta_p = 40cP$, (c) $\eta_n = 400cP$, $\eta_p = 40cP$, (d) $\eta_n = 400cP$, $\eta_p = 400cP$. η_p and η_n are the viscosities of the platelet aggregate and fibrin network, respectively, (e) Dynamics of total volumes of the clot. Blue triangle: $\eta_n = 4cP$, $\eta_p = 40cP$. Red circle: $\eta_n = 400cP$, $\eta_p = 400cP$.

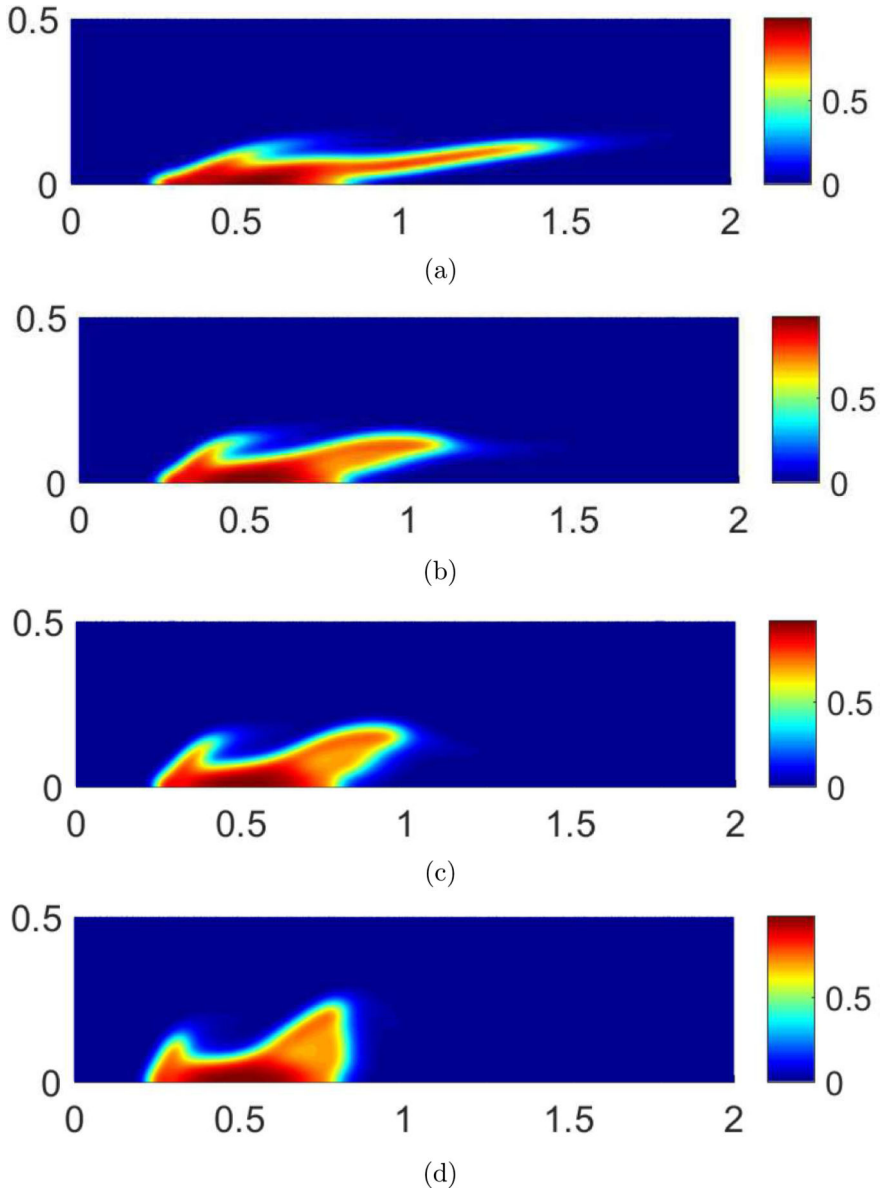

Figure 9:

Shapes of clots with different values of elasticity modulus described by steady state solutions of the model system of equations, (a) $\lambda_n = 0.1Pa$, $\lambda_p = 1Pa$. (b) $\lambda_n = 1Pa$, $\lambda_p = 10Pa$. (c) $\lambda_n = 10Pa$, $\lambda_p = 10Pa$. (d) $\lambda_n = 50Pa$, $\lambda_p = 10Pa$. λ_p and λ_n are elasticity moduli of the platelet aggregates and fibrin networks, respectively.

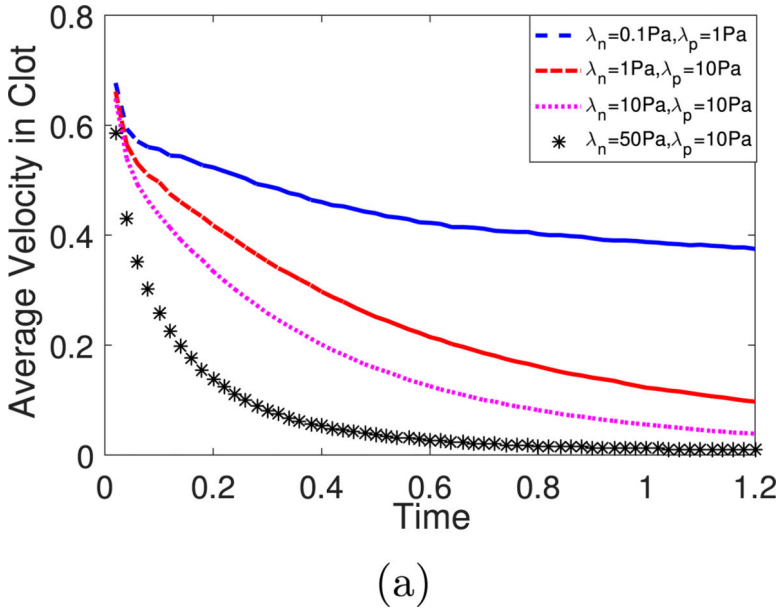

Figure 10:

Evolution of averaged velocity inside clot $\int_\Omega \chi_{Clot}|\boldsymbol{u}|d\boldsymbol{x}/\int_\Omega \chi_{Clot}d\boldsymbol{x}$. λ_p and λ_n are elasticity moduli of the platelet aggregates and fibrin networks, respectively.

Table 1:

The parameters used in convergence study.

Re	l_s	ϵ	α	β_g
0.1	0.005	0.01	10	20

Here Re is the Reynolds number; l_s is the slip length; $\epsilon = 0.01$ is the capillary width; $\alpha = \frac{\lambda_A L}{\eta_A U}$ is the mixture energy coefficient; $\beta_g = \frac{\rho_A g L^2}{\eta_A U} = 20$ is the gravitational force.